Article Open Access | Vita

Simian-specific SAGE1 enhances germline genome stability by promoting homologous recombination

Jingzheng Li[1,2#], Xiaozhu Wang[2#], Futang Wan[2#], Fanyang He[1,2#], Huaisheng Lu[2], Xidan Miao[2], Juan Chen[2], Jiahui Guo[1,2], Lili Zhuang[2], Yanan Hou[2], Tingyi Wei[2], Biying Chen[1,2], Zhouliang Bian[1,2], Hongjuan Chai[3], Qing Ren[3], Xin Gu[4], Bin Xu[4], Hanlin Zeng[2], Qian Bian[2], Jian Wu[2], Chenhui Huang[*2], Yanjie Zhang[*1,2], Ming Lei[*2,5,6]

DNA damage response (DDR) is essential for maintaining germline genome integrity to ensure the accurate transmission of genetic information. Most DDR genes emerged at an early evolutionary stage and had been acquired by the time the *Vertebrata* group first arose. Here, we identify a spermatogonia-enriched protein encoded by *SAGE1*, a simian-specific X-linked gene, as a recently evolved DDR regulator that plays an essential role in maintaining germline genome stability. The unique *SAGE1*-specific exon repeats endow SAGE1 with the ability of promoting germline genome integrity via the error-free homologous recombination (HR) pathway by orchestrating crucial repair steps through multiple interactions with key HR factors, such as CtIP, SOSS and NuA4 complexes. Thus, SAGE1 represents an 'upgrade' to the existing landscape of DDR by introducing an additional layer of regulation. Our findings provide novel insights into the evolutionary adaptations underlying distinctive traits of simians, suggesting that SAGE1 might be one of the key genetic underpinnings for the enhanced germline genome integrity in the simian lineage.

https://doi.org/10.15302/vita.2026.05.0034

INTRODUCTION

DNA damage poses a major threat to genome stability, and cells have therefore evolved elegant mechanisms, collectively referred to as the DNA damage response (DDR), to protect genome integrity[1,2]. Among various types of damages, double-strand break (DSB) is one of the most severe types of DNA lesions, eliciting a rapid and robust DDR[3-5]. DSBs are repaired through two primary pathways, accurate homology-directed repair (HR) and error-prone non-homologous end joining (NHEJ)[5-9]. Most DDR-related genes including those in the HR and NHEJ pathways (~70%) had been acquired when the Eukaryota split occurred, and the incorporation of new genes had been by and large established by the time the *Vertebrata* group appeared, with only a few subsequent innovations detected[10-13]. One of the most recent additions to the DDR landscape is the Shieldin complex, which promotes the NHEJ pathway for the repair of DSBs, and may have contributed to the evolution of antibody class-switch recombination in amphibians[14-18]. This raises an intriguing question whether the emergence of advanced DDR-related traits during evolution could be mechanistically linked with the birth of some novel DDR factors.

Spermatogonia (SPG) are essential for male fertility as they ensure a continuous supply of sperms throughout a male's reproductive lifespan[19,20]. Although efficient DDRs are essential for reducing damage-related mutations in all cell types, they particularly ensure the accurate transmission of genetic information to the next generation[20-27]. This is manifested in the significantly lower mutation rate of germline compared to somatic cells[21,28-30], suggesting that DNA surveillance and repair must be optimized in germline cells to minimize spontaneous mutations and mitigate the risk of extinction. Notably, pedigree-based studies demonstrate that the mutation rate in human germlines is significantly lower than that in mouse germlines, indicating that human germ cells are more efficient at maintaining genome integrity[31]. However, the underlying mechanism remains largely elusive. Primates have evolved a set of novel genes that are preferentially expressed during spermatogenesis, yet their functions remain poorly understood[32]. We posit that primates might have evolved novel DDR factors to enhance their germline genome integrity. Identification and characterization of such novel, primate-specific DDR genes present a major challenge for the fields of DNA damage repair, evolution, and reproduction biology.

Here, we identify a spermatogonia-enriched protein encoded by *SAGE1*, a simian-specific X-linked gene, as a recently evolved DDR regulator. Mechanistically, SAGE1 is recruited to DSB sites directly via the interaction between its specific exon repeats and the MRN-CtIP complex, facilitating SOSS complex stability and promoting resection at DSBs. SAGE1 also recruits the NuA4 complex, triggering TIP60-mediated acetylation of H4K16. This acetylation inhibits 53BP1 localization and suppresses the NHEJ pathway. Collectively, the action of SAGE1 at DSBs enhances the HR pathway while reducing the NHEJ activity, promoting simian germline genome integrity.

---

1. Department of Oncology, Ninth People's Hospital, Shanghai Jiao Tong University School of Medicine, Shanghai, China. 2. Shanghai Institute of Precision Medicine, Ninth People's Hospital, Shanghai Jiao Tong University School of Medicine, Shanghai, China. 3. Department of Obstetrics and Gynecology, Ninth People's Hospital, Shanghai Jiao Tong University School of Medicine, Shanghai, China. 4. Department of Urology, Ninth People's Hospital, Shanghai Jiao Tong University School of Medicine, Shanghai, China. 5. State Key laboratory of Oncogenes and Related Genes, Shanghai Jiao Tong University School of Medicine, Shanghai, China. 6. Shanghai Academy of Natural Sciences (SANS), Shanghai, China. #These authors contributed equally. *Correspondence: Chenhui Huang (huangchh@shsmu.edu.cn), Yanjie Zhang (zhangyanjie@shsmu.edu.cn), Ming Lei (leim@shsmu.edu.cn)

Received: October 28, 2025; Accepted: May 8, 2026; Published: May 25, 2026

RESULTS

SAGE1 promotes simian spermatogonia genome stability

To investigate the difference in germline DDR between primates and rodents, we isolated cells from human (*Homo sapiens*), crab-eating macaque (*Macaca fascicularis*), and mouse (*Mus musculus*) testicular tissues for immunofluorescence (IF) analysis. Given that a major threat to SPG is the DNA damage during the S phase, we specifically compared the DDR in cycling SPG. We co-stained primary germ cells with SPG markers (PLZF/SALL4 for mouse; UTF1/MAGE-A4 for primate), Cyclin A2 (S/G2 phase marker), and γH2AX (DNA damage marker) following treatment with etoposide or hydroxyurea (HU). Quantification of the γH2AX intensity exclusively in Cyclin A2-positive SPG revealed that cycling mouse SPG (*Mm*SPG) exhibited significantly higher levels of DNA damage compared to cycling macaque (*Mf*SPG) and human (*Hs*SPG) SPG, indicating that the genomic stability of cycling *Mm*SPG is more vulnerable to the DNA-damaging agents (Fig. 1a, b; Supplementary Fig. S1a).

Next, we set out to investigate what novel mechanism governs this primate-specific mode of DDR. We hypothesized that newly evolved genes, unique to primates, might constitute the genetic basis for enhanced genome stability in cycling SPG. Notably, a systematic mapping of the neighborhood network of core human DDR factors revealed a previously uncharacterized *SAGE1* as the sole primate SPG-specific entry enriched with at least two baits among *BRCA1*, *53BP1* and *DMC1* (Fig. 1c)[14,32,33]. Human *SAGE1* and its homologous genes are located on the long arm of the X chromosome, directly adjacent to a tandem array of *CT45A* genes (Fig. 1d). Together, *SAGE1* and *CT45A* form a gene locus flanked by two single-copy genes, *INTS6L* and *MMGT1* (Fig. 1d). Intriguingly, *SAGE1* is absent from the *INTS6L-MMGT1* synteny block in prosimians, rodents, and all other placental mammals (Fig. 1d; Supplementary Fig. S2a–c and Data S1). Immunohistochemistry demonstrates that SAGE1 is expressed in the nuclei of SPG and round spermatids under physiological conditions (Supplementary Fig. S3a). Moreover, IF analysis of testicular tissue showed co-expression of SAGE1 with the SPG marker MAGE-A4 and the proliferation marker Ki67, while the SAGE1 signal was not detected in spermatocytes (Supplementary Fig. S3b, c). To further elucidate SAGE1 expression across the stages of spermatogonial development, we enriched primary SPG from human and macaque testes and performed scRNA-seq analyses. The result revealed an enriched *SAGE1* expression in undifferentiated and differentiating SPG, with a pattern concordant with Ki67 and SPG markers, including *MAGE-A4*, *UTF1*, and *SALL4* (Supplementary Fig. S4a–e)[33,34]. Taken together, these data indicate that SAGE1 is a newly evolved, simian-specific DDR factor that may account for the enhanced SPG genome stability.

To test this hypothesis, we first evaluated the potential contribution of SAGE1 to germline genomic stability in simians. Knocking down *SAGE1* in *Hs*SPG using shRNA (Supplementary Fig. S5a) resulted in accumulated DNA damages, as evidenced by the increased γH2AX signals (Fig. 1e). In addition, overall DSB repair efficiency was prominently impaired in *SAGE1*-knockdown *Hs*SPG (Fig. 1f). These analyses support the notion that SAGE1 plays an essential role in safeguarding genome stability in *Hs*SPG. Intriguingly, *SAGE1*-depleted *Hs*SPG exhibited decreased RAD51 foci and increased 53BP1 recruitment at DSB sites following etoposide treatment (Fig. 1g, h). Given that RAD51 and 53BP1 are emblematical factors for the HR and NHEJ pathways respectively, these findings provide a mechanistic insight that SAGE1 is required for maintaining human germline genome stability via the error-free HR pathway in DSB processing. Consistent with this, *SAGE1* knockdown in *Mf*SPG yielded the same phenotypes, underscoring the evolutionarily conserved DDR function of SAGE1 in simians (Supplementary Fig. S5b–d).

SAGE1 promotes spermatogonia DSB repair *in vivo*

To further explore the *in vivo* role of SAGE1 in maintaining germline genome stability, we performed loss- and gain-of-function analyses in non-human primate, mouse and *Drosophila* SPG. *SAGE1* knockdown was achieved in crab-eating macaque testes by adeno-associated virus serotype 9 (AAV9) delivered shRNA (Supplementary Fig. S6a, b). Following organotypic testis culture and cisplatin treatment, testis slices were subjected to IF staining. Although γH2AX signals of spermatocytes were similar in sh*Ctrl* and sh*SAGE1* testes (Supplementary Fig. S6c), a much more severe accumulation of γH2AX in MAGE-A4 positive SPG was observed in sh*SAGE1* testis compared to sh*Ctrl* testis (Fig. 1i; Supplementary Fig. S3c), suggesting that SAGE1 provides a protection against DNA damages in simian SPG.

In the gain-of-function assays, *HsSAGE1*$^{flox/+}$*/Vasa-Cre* mouse model (hereafter referred to as *HsSAGE1*-vKI) (Supplementary Fig. S7a–c) was generated to ectopically express human SAGE1 (*HsSAGE1*) in mouse SPG (Supplementary Fig. S7d)[35,36]. Upon ionizing radiation (IR) exposure, significantly lower γH2AX signals were observed in Sall4-positive SPG of *HsSAGE1*-vKI mice compared to control testes, while the γH2AX signals in spermatocytes remained unaffected (Sall4, a mouse SPG marker; Fig. 1j and Supplementary Fig. S7e). In addition, we also ectopically expressed *HsSAGE1* in *Drosophila* SPG cells using the germ cell-specific Nanos-Gal4 driver (Supplementary Fig. S8a, b)[37]. IF staining confirmed the specific expression of *Hs*SAGE1 in these cells (Supplementary Fig. S8c). IR induced marked DNA damage (γH2Av) and apoptosis (cleaved caspase-3, CC3) in wild-type (WT) testes, but this response was significantly blunted in *Hs*SAGE1-expressing SPGs (Supplementary Fig. S8d, e). These gain-of-function assays demonstrated that mouse and *Drosophila* SPG equipped with human SAGE1 acquired an improved ability to repair DSBs. Taken together, these *in vivo* data corroborate our *in vitro* phenotypic observations and suggest that SAGE1 provides a substantial protection against DNA damages and likely contributes to the enhanced genome stability in simian SPG.

Simian-specific tandem SAGE1-specific exon repeats (SERs) enable SAGE1 to safeguard spermatogonia genomic stability

To gain more mechanistic insights into how SAGE1 increases germline genome stability in simians, we analyzed the genetic sequence and the domain organization of SAGE1. Multiple sequence alignment unveiled conserved N- and C-terminal domains (NTD and CTD) shared by SAGE1 and its adjacent CT45A, indicative of a paralogous relationship among these proteins (Fig. 2a; Supplementary Fig. S9a). Notably, our analysis also revealed highly repetitive motifs in the central region of *SAGE1* across simian species, which are absent in the CT45A (Fig. 2a; Supplementary Fig. S9a–c). Gene structure analysis further indicated that these repetitive motifs are encoded by tandem exons in simian *SAGE1* genes, and are henceforth referred to as SERs (Fig. 2a; Supplementary Fig. S9d). These

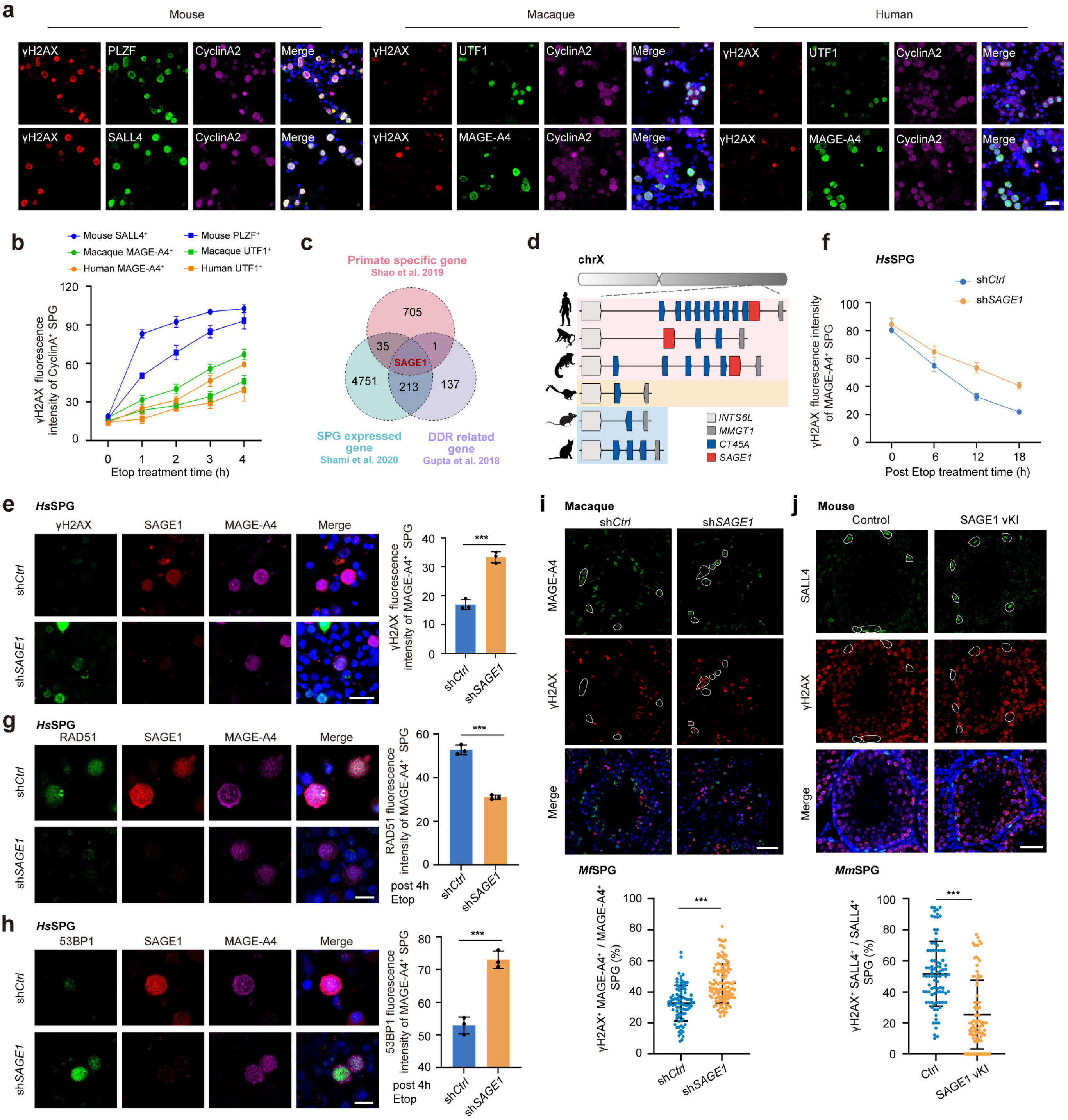

Fig. 1 **SAGE1 promotes simian spermatogonia genome stability.** **a** Representative IF images of primary germ cells from human, crab-eating macaque, and mouse testicular tissues stained with antibodies against SPG markers (*Mm*SPG: PLZF, SALL4; *Mf*SPG and *Hs*SPG: UTF1, MAGE-A4), Cyclin A2 (S/G2 marker) and γH2AX after 2 h etoposide (10 µM) treatment. Scale bar, 20 µm. $n = 3$ independent replicates with at least 100 cells per condition. **b** The quantification of γH2AX fluorescence intensity of cycling SPG shown in **a**. **c** Venn diagram depicting the overlap among DDR-related genes (purple)[14], primate-specific genes (pink)[32], and spermatogonia-expressing genes (blue)[33]. *SAGE1* is the only gene found at the intersection of all three gene sets. **d** Gene order within the *INTS6L-MMGT1* synteny block of human (*Homo sapiens*), crab-eating macaque (*Macaca fascicularis*), marmoset (*Callithrix jacchus*), mouse lemur (*Microcebus murinus*), mouse (*Mus musculus*) and cat (*Felis catus*). **e** Representative IF images of sh*Ctrl* and sh*SAGE1* *Hs*SPG stained with antibodies against MAGE-A4, SAGE1 and γH2AX, with the quantification shown on the right. Scale bar, 20 µm. $n = 3$ independent replicates with at least 100 cells per condition. **f** The quantification of γH2AX fluorescence intensity of cycling sh*Ctrl* and sh*SAGE1* *Hs*SPG by IF staining. $n = 3$ independent replicates with at least 100 cells per condition. **g** Representative IF images of sh*Ctrl* and sh*SAGE1* *Hs*SPG stained with antibodies against MAGE-A4, SAGE1 and RAD51 after 4 h etoposide (10 µM) treatment, with the quantification shown on the right. Scale bar, 10 µm. $n = 3$ independent replicates with at least 100 cells per condition. **h** Representative IF images of sh*Ctrl* and sh*SAGE1* *Hs*SPG stained with antibodies against MAGE-A4, SAGE1 and 53BP1 after 4 h etoposide (10 µM) treatment, with the quantification shown on the right. Scale bar, 10 µm. $n = 3$ independent replicates with at least 100 cells per condition. **i** Representative IF images of γH2AX and MAGEA4 staining in sh*Ctrl* and sh*SAGE1* macaque testes at 4 h after 2 h cisplatin treatment, with the quantification shown on the right. Scale bar, 50 µm. sh*Ctrl* and sh*SAGE1*, $n = 88$, 120 seminiferous tubules from two macaque testes. **j** Representative IF images of γH2AX and SALL4 staining in Control and *SAGE1*-vKI mouse testes at 5 h after 1 Gy irradiation, with the quantification shown on the right. Scale bar, 50 µm. Control and *SAGE1*-vKI, $n = 91$, 93 seminiferous tubules from 3 mouse testes. For all experiments, data are shown as mean ± SD. Significance was determined with two-tailed Student's *t*-test. ***$P < 0.001$.

analyses suggest that it might be the newly evolved SERs that confer a novel function to the *SAGE1* genes to promote the germline genome stability in simians.

To test this idea, we delivered WT *HsSAGE1* and a mutant *HsSAGE1* devoid of SERs (*HsSAGE1*$_{\Delta SER}$) into *Mm*SPG cells (Supplementary Fig. S10a). We found that ectopic *HsSAGE1* expression indeed increased the repair ability of *Mm*SPG treated with etoposide (Fig. 2b). Moreover, etoposide treatment led to increased RAD51 and decreased 53BP1 foci in *Hs*SAGE1-expressing *Mm*SPG cells compared with the control cells (Fig. 2c, d; Supplementary Fig. S10b, c). In stark contrast, *HsSAGE1*$_{\Delta SER}$ failed to enhance the protection of *Mm*SPG germline genome stability from the genotoxic insults (Fig. 2b–d; Supplementary Fig. S10b, c). Furthermore, *HsSAGE1*-expressing mouse embryonic fibroblast (MEF) cells also showed dramatically reduced frequency of chromosomal aberration formation as compared to *HsSAGE1*$_{\Delta SER}$ MEF after cisplatin treatment (Fig. 2e). Together, these data demonstrate that tandem SERs endow *Hs*SAGE1 with the ability of promoting germline genomic stability likely via the HR pathway.

To obtain further evolutionary insights into the functional significance of the tandem SERs, human *SAGE1* or its homologous genes from different species along the evolutionary trajectory were ectopically expressed in mouse MEFs and evaluated for their abilities in maintaining the genome stability (Supplementary Fig. S10d). Expression of human, crab-eating macaque, and common marmoset (*Callithrix jacchus*)

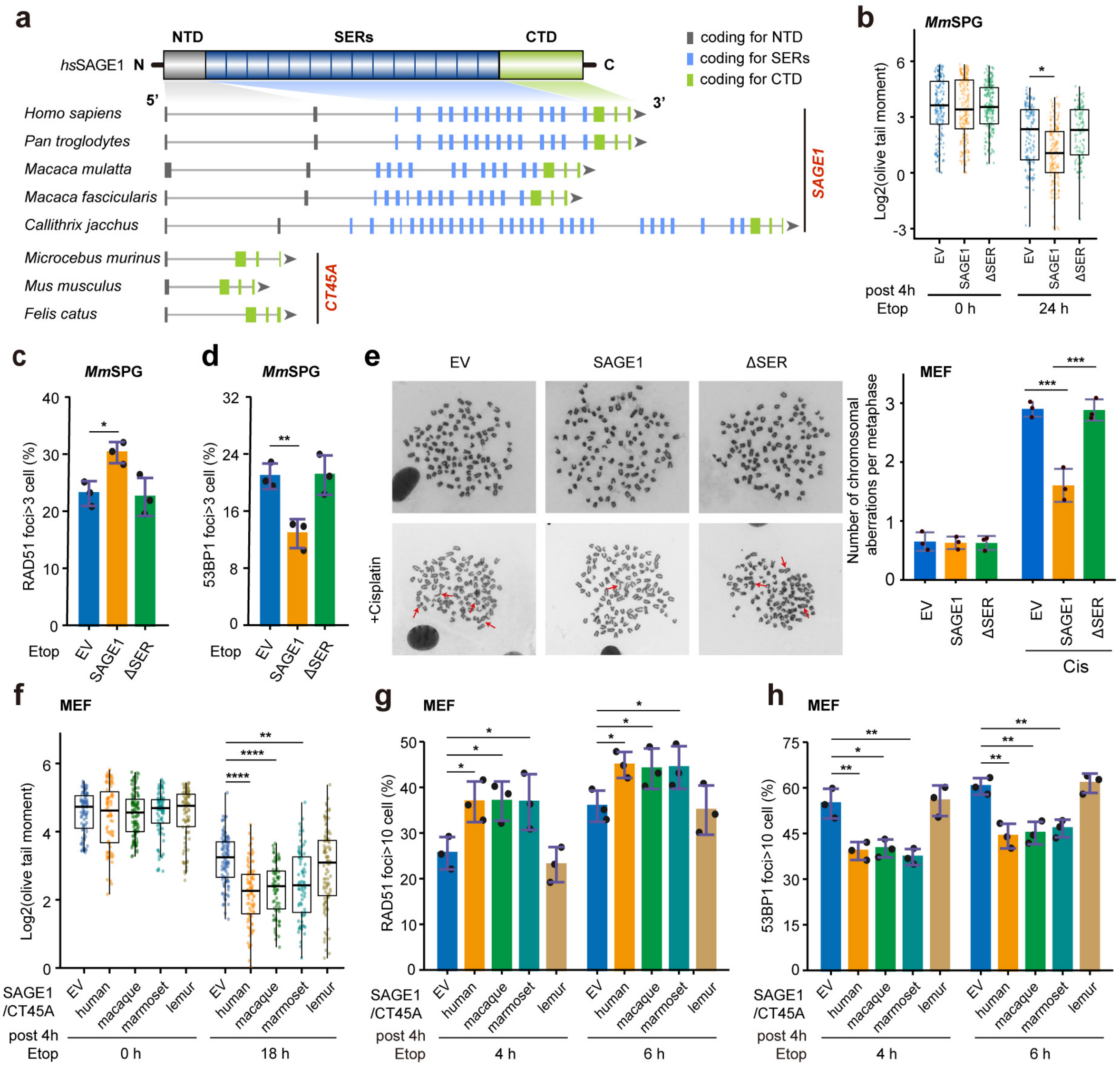

Fig. 2 Simian-specific tandem SERs of SAGE1 promote spermatogonia genome stability. a Schematic diagrams of *SAGE1* and its paralogous *CT45A* genes across mammalian species. N-terminal domains (NTD) are colored in grey, SERs in light blue, and the C-terminal domain (CTD) in light green. **b** *Mm*SPG were infected with lentivirus carrying empty vector (EV), human *SAGE1*, or human *SAGE1* mutant devoid of SERs (ΔSER). The neutral comet assay was performed to analyze DSBs at 0 h and 24 h post-etoposide (10 μM) treatment. *n* = 100 cells per condition were analyzed. **c, d** Quantification of RAD51 (**c**) and 53BP1 (**d**) positive cells (foci > 3) in *Mm*SPG ectopically expressing EV, *Hs*SAGE1, or *Hs*SAGE1$_{\Delta SER}$ after 4 h etoposide (10 μM) treatment, respectively. *n* = 3 independent replicates with at least 100 cells per condition. **e** Quantification of chromosome abnormalities in ectopically expressing EV, *Hs*SAGE1, or *Hs*SAGE1$_{\Delta SER}$ MEF, either treated with cisplatin (0.5 μM) or untreated. *n* = 3 independent replicates with at least 50 cells per condition. Representative images of metaphase spreads derived from the indicated MEFs. Arrows point to representative abnormal chromosomes. **f** MEF cells were transfected with EV, SAGE1 from human, macaque, marmoset, or CT45A from mouse lemur. The neutral comet assay was performed to analyze DSBs at 0 h and 18 h post etoposide (10 μM) treatment. *n* = 100 cells per condition. **g, h** Quantification of RAD51 (**g**) and 53BP1 (**h**) positive cells (foci > 10) in MEF ectopically expressing EV, SAGE1 from human, macaque, marmoset, or CT45A from mouse lemur after 4 h etoposide (10 μM) treatment. *n* = 3 independent replicates with at least 100 cells per condition. For all experiments, data are shown as mean ± SD. Significance was determined with two-tailed Student's *t*-test. $^{*}P < 0.05$, $^{**}P < 0.01$, $^{***}P < 0.001$, $^{****}P < 0.0001$.

SAGE1 all showed a protection of the genome integrity from the effects of etoposide treatment, while in contrast expression of the paralogous gene *CT45A* from mouse lemur (*Microcebus murinus*, a prosimian) that lacks tandem SERs did not show any protective effects (Fig. 2f). In *HsSAGE1*-, *MfSAGE1*-, and *CjSAGE1*-expressing cells, the RAD51 foci were clearly stimulated, accompanied by the reduction of 53BP1 foci (Fig. 2g, h; Supplementary Fig. S10e, f). While in mouse lemur CT45A-expressing cells, the levels of RAD51 and 53BP1 foci in response to etoposide were similar to those in the control cells (Fig. 2g, h; Supplementary Fig. S10e, f). In aggregate, these results support the notion that, once the tandem SERs evolutionarily emerged in SAGE1 in the common ancestor of simians, the SAGE1 gene likely had simultaneously acquired the aptness to enhance the germline genome stability.

Tandem SERs mediate SAGE1 recruitment to DSBs to promote HR

In order to illuminate the mechanism of how SAGE1 participates in DDR, we examined its dynamic distribution upon genotoxic stimuli. SAGE1 proteins were diffusely distributed throughout the nuclei in *Hs*SPG and *Mf*SPG under normal conditions, but aggregated to form bright foci that colocalized with γH2AX signals upon etoposide treatment, indicating that SAGE1 is directly involved in the DDR process (Fig. 3a). As a cancer-testis antigen (CTA) gene, *SAGE1* is often aberrantly reactivated in a range of cancer types (Supplementary Fig. S11a, b). We verified its expression in multiple cancer cells from different tissue origins, including U-2 OS osteosarcoma, HuTu-80 human duodenal adenocarcinoma, A375 melanoma, and HCC-P primary sarcomatoid hepatocellular carcinoma (Supplementary Fig. S11c). Notably, the protein level of SAGE1 in these cells was markedly upregulated and substantially enriched on chromosomes at the DNA damage sites in response to genotoxic stresses, indicative of a direct connection of SAGE1 in the DDR process in SAGE1-positive cancer cells (Supplementary Fig. S11c, d). In addition, knockdown of *SAGE1* in HuTu-80 cells gave rise to the same DDR phenotypes as those observed in *Hs*SPG (Supplementary Fig. S11e–h). The chromosome instability phenotypes including chromosome breaks and chromosome translocation measured by sister chromatid exchange (SCE), were prevalent in *SAGE1*-knockdown cells compared to control (Supplementary Fig. S12a, b). Taken together, these results underscored that the function of SAGE1 in preserving genomic stability is an intrinsic characteristic, applying to all SAGE1-expressing cells.

To monitor the dynamics of SAGE1 in response to DNA damages, we introduced EGFP-tagged WT human SAGE1 and two complementary deletion mutants, $\mathrm{SAGE1_{SER}}$ and $\mathrm{SAGE1_{\Delta SER}}$, into HuTu-80 cells and micro-irradiated the nuclei using a 405 nm laser to induce DSBs. Within 30 seconds, fluorescent signals quickly accumulated at the irradiated areas in SAGE1-expressing cells, and soon reached the maximum level about 10 min after the irradiation (Fig. 3b, c). Strikingly, $\mathrm{SAGE1_{SER}}$ that only contains the tandem SERs exhibited the same dynamics as WT SAGE1, whereas the complementary mutant $\mathrm{SAGE1_{\Delta SER}}$ failed to load onto the damage sites but instead localized in the nucleoli unresponsive to DNA damages (Fig. 3b, c; Supplementary Fig. S12c). These results suggest that the SERs confer upon SAGE1 the capacity for rapid DDR recruitment, a property that may be co-opted in both germline and aberrantly SAGE1-expressing cancer cells to enhance HR-mediated repair.

Next, we adopted two well-established GFP-based reporter systems, DR-GFP and EJ5-GFP[38], to further quantify the impacts of SAGE1 on the HR and NHEJ repair pathways, respectively (Fig. 3d, e). Upon the inducible expression of I-SceI endonuclease in U-2 OS cells, SAGE1 was significantly enriched at the I-SceI-induced DSB sites, as revealed by chromatin immunoprecipitation (ChIP)-qPCR analysis (Fig. 3d, e). HR activity was substantially decreased in SAGE1-depleted U-2 OS cells, accompanied by an elevated NHEJ frequency (Fig. 3f; Supplementary Fig. S12d). Consistently, SAGE1 loss significantly impeded the localization of RAD51 to DSBs, but elicited more 53BP1 loading onto the damage sites in HuTu-80 cells (Supplementary Fig. S11g, h). Ectopic expression of WT SAGE1 but not the SER deletion mutant led to both HR activation and NHEJ suppression in MEF cells (Fig. 3g; Supplementary Fig. S12e), further confirming that SAGE1 facilitates the error-free repair pathway to shield the genome from lesions.

To examine whether the effect of SAGE1 on DSB repair is cell-cycle dependent, we arrested HuTu-80 cells at the G1 phase by double-thymidine treatment and then released them to the S/G2 phases (Fig. 3h). Clearly, attenuation of NHEJ by SAGE1 was cell cycle-independent, whereas SAGE1's effect on HR was confined to the S/G2 phases, aligning with the fact that HR mainly occurs in these phases (Fig. 3i). Collectively, these data demonstrate that SAGE1 is an early DDR regulator that is recruited to the damage sites via its tandem SERs to promote error-free HR and suppress error-prone NHEJ pathways to maintain genome fidelity.

Tandem SERs mediate SAGE1 interaction with CtIP at DSBs to facilitate end resection

The MRE11–RAD50–NBS1 (MRN) complex, an essential early factor of DDR, plays key roles in sensing DSBs, initiating DNA end resection, and directing DDR to the HR pathway[39-41]. This prompted us to ask whether the MRN complex is required for the quick recruitment of SAGE1 to the DNA damage sites. Ablation of MRE11 and NBS1 in HuTu-80 cells significantly attenuated the SAGE1 recruitment at the laser-induced DSB stripes, whilst depletion of SAGE1 exhibited no impact on the accumulation of either MRE11 or NBS1 at the damage sites, indicating that SAGE1 lies downstream of the MRN complex in the DDR process (Fig. 4a; Supplementary Fig. S13a–d).

A critical event in HR is MRN-mediated recruitment of CtIP (C-terminal binding protein interacting protein) to the DSB sites, which in turn stimulates the nuclease activity of the MRN complex for DNA end resection[42-44]. In accordance with this intimate MRN–CtIP connection, knocking down CtIP greatly blocked SAGE1 accumulation at DNA damage sites (Fig. 4a). But intriguingly, damage site accumulation of CtIP was also reduced in SAGE1-depleted cells, raising the possibility of a close tie between SAGE1 and CtIP (Fig. 4b). In line with this idea, endogenous SAGE1 and CtIP proteins could reciprocally immunoprecipitate each other in HuTu-80 cells, and this connection was augmented in the presence of DNA damages (Fig. 4c). Of note, co-immunoprecipitation (co-IP) analysis revealed that this SAGE1–CtIP interaction relies on the tandem SERs (primarily $\mathrm{SER_{13}}$) of SAGE1 and the central region of CtIP (Fig. 4d–f; Supplementary Fig. S13e). Further characterization using purified materials demonstrated that SERs 11–14 of SAGE1 ($\mathrm{SAGE1_{SER11-14}}$) could mediate a stable, direct interaction with a 282-residue fragment of CtIP (residues 509–790), hereafter referred to as the SAGE1-inter-

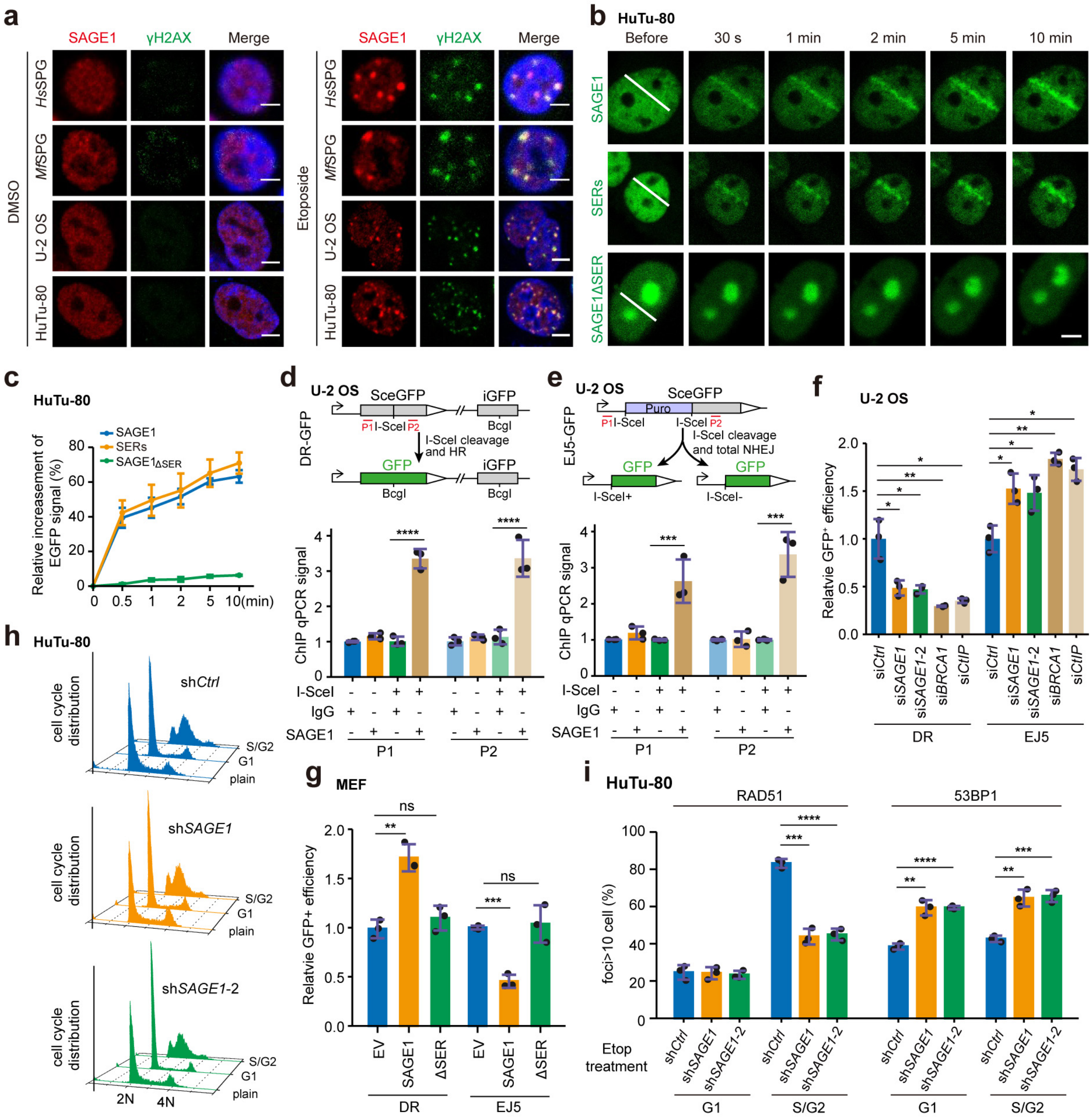

Fig. 3 **Tandem SERs mediate SAGE1 recruitment to DSBs to promote HR.** **a** IF analysis of SAGE1 and γH2AX co-localization in *Hs*SPG, *Mf*SPG, U-2 OS, and HuTu-80 cells treated with DMSO or 10 µM etoposide. Scale bars, 2.5 µm (SPG) and 5 µm (U-2 OS, HuTu-80). **b** HuTu-80 cells were transfected with plasmids carrying SV40 NLS motif- and EGFP-tagged SAGE1, SAGE1$_{\mathrm{SER}}$ or SAGE1$_{\Delta\mathrm{SER}}$, and stripped by laser. Real-time EGFP recruitment was monitored by confocal microscopy. Scale bar, 5 µm. **c** Quantification of panel (**b**), *n* = 10 cells were analyzed. **d, e** Schematic diagrams of the DR-GFP (HR) (**d**) and EJ5-GFP (NHEJ) (**e**) assays (upper panel). DR-GFP (**d**) and EJ5-GFP (**e**) labeled U-2 OS cells were transfected with blank or I-SceI expressing plasmid. ChIP-qPCR was performed 24 h after transfection to analyze SAGE1 enrichment at I-SceI-induced DSB sites. *n* = 3 independent replicates. **f** 24 h after si*SAGE1* transfection, DR-GFP and EJ5-GFP U-2 OS cells were transfected with I-SceI plasmid. FACS was performed 48 h later to analyze GFP expression. *n* = 3 independent replicates. **g** DR-GFP or EJ5-GFP plasmid and I-SceI plasmid were co-transfected in MEF cells ectopically expressing EV, *Hs*SAGE1, or *Hs*SAGE1$_{\Delta\mathrm{SER}}$. FACS was performed 48 h later to analyze GFP expression. *n* = 3 independent replicates. **h** Flow-cytometry analysis of sh*Ctrl* and sh*SAGE1* HuTu-80 cells after double-thymidine treatment. **i** Quantification of co-localization of RAD51 and 53BP1 with γH2AX in sh*Ctrl* and sh*SAGE1* HuTu-80 cells at the G1 and S/G2 phases after 4 h etoposide (10 µM) treatment. *n* = 3 independent replicates with at least 100 cells per condition. For all experiments, data are shown as mean ± SD. Significance was determined with two-tailed Student's *t*-test. $^{*}P < 0.05$, $^{**}P < 0.01$, $^{***}P < 0.001$, $^{****}P < 0.0001$.

acting motif of CtIP (CtIP$_{\mathrm{SIM}}$) (Fig. 4g; Supplementary Fig. S13f, g). Consistent with these biochemical data, the impaired CtIP loading onto DSBs in SAGE1-knockdown cells was restored by the expression of shRNA-resistant WT SAGE1 but not the SAGE1$_{\Delta\mathrm{SER}}$ mutant (Fig. 4h). Taken together, these results show that the tandem SERs of SAGE1 mediate the direct binding and mutual reinforcement of SAGE1 with CtIP, explaining how SAGE1 is quickly recruited to the DNA damage sites.

To explore the role of the SAGE1–CtIP interaction in DNA end resection, we monitored the formation of ssDNA at DSBs in SAGE1-knockdown cells. Upon etoposide treatment, bromodeoxyuridine (BrdU)-labeled ssDNA foci and the recruitment of RPA (Replication Protein A) at DSB sites were evident in control cells, but was substantially reduced in SAGE1 depleted cells (Fig. 4i, j). Ectopically expressing shRNA-resistant WT SAGE1 but not SAGE1$_{\Delta\mathrm{SER}}$ that lacks the ability to

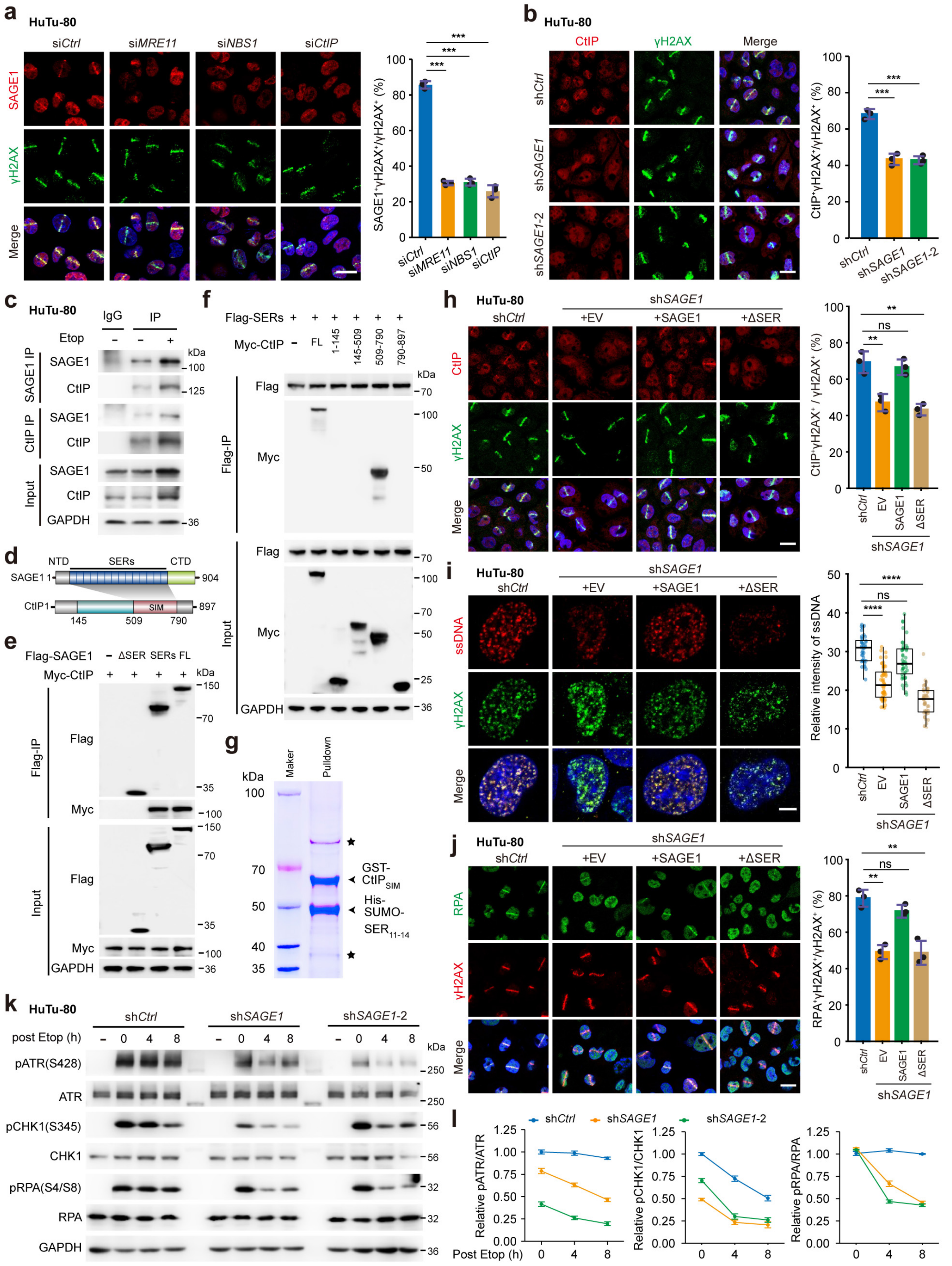

Fig. 4 Tandem SERs mediate SAGE1 interaction with CtIP at DSBs to facilitate end resection. a IF analysis of SAGE1 and γH2AX co-localization at laser stripes in si*Ctrl*, si*MRE11*, si*NBS1*, and si*CtIP* HuTu-80 cells, with the quantification shown on the right. Scale bar, 20 μm. *n* = 3 independent replicates with at least 100 cells per condition. **b** IF analysis of CtIP and γH2AX co-localization at laser stripes in shCtrl, sh*SAGE1*, sh*SAGE1*-2 HuTu-80 cells, with the quantification shown on the right. Scale bar, 20 μm. *n* = 3 independent replicates with at least 100 cells per

condition. **c** Reciprocal immunoprecipitation (IP) of SAGE1 and CtIP using cell lysates from HuTu-80 cells with or without etoposide treatment. **d** Schematic diagrams of SAGE1 and CtIP protein organizations highlighting the interacting domains. **e** Co-IP experiments in HEK293T cells co-transfected with plasmids expressing Myc-CtIP and various Flag-SAGE1 truncations. FL: full-length. **f** Co-IP experiments in HEK293T cells co-transfected with plasmids expressing Flag-SAGE1$_{\mathrm{SER}}$ and various Myc-CtIP truncations. **g** Two-step affinity purification of the [GST-CtIP$_{\mathrm{SIM}}$]–[His-SUMO-SAGE1$_{\mathrm{SER11-14}}$] complex. The Coomassie-stained SDS-PAGE shows the complex after the two-step affinity purification. Corresponding bands are labeled, and contaminating proteins are denoted by asterisks. **h** Representative IF images of CtIP and γH2AX in laser-microirradiated sh*Ctrl*, sh*SAGE1*+EV, sh*SAGE1*+SAGE1, and sh*SAGE1*+ΔSER HuTu-80 cells, with co-localization quantified on the right. Scale bar, 20 μm. *n* = 3 independent replicates with at least 100 cells per condition. **i** Representative IF images of ssDNA and γH2AX in etoposide treated sh*Ctrl*, sh*SAGE1*+EV, sh*SAGE1*+SAGE1, and sh*SAGE1*+ΔSER HuTu-80 cells, with the quantification shown on the right. Scale bar, 5 μm. *n* = 40 cells per condition. **j** Representative IF images of RPA and γH2AX in laser-microirradiated sh*Ctrl*, sh*SAGE1*+EV, sh*SAGE1*+SAGE1, and sh*SAGE1*+ΔSER HuTu-80 cells, with co-localization quantified on the right. Scale bar, 20 μm. *n* = 3 independent replicates with at least 100 cells per condition. **k** sh*Ctrl* and sh*SAGE1* HuTu-80 cells were treated with 10 μM etoposide for 4 h and released for indicated time periods. ATR-CHK1 signaling was analyzed by western blot. **l** The quantification of phosphorylated protein levels in panel (**k**). For all experiments, data are shown as mean ± SD. Significance was determined with two-tailed Student's *t*-test. $^{**}P < 0.01$, $^{***}P < 0.001$, $^{****}P < 0.0001$.

interact with CtIP successfully restored the ssDNA and RPA signals, indicating that SER-mediated SAGE1-CtIP interaction is required for both resection initiation and processing (Fig. 4i, j). Protein kinase ATR (ataxia telangiectasia mutated and Rad3-related) activation by ssDNA elicits CHK1 phosphorylation to regulate cell cycle checkpoints and DNA repair processes[44,45]. Accordant with the decrease in ssDNA generation, *SAGE1* knockdown led to a significant attenuation of the ATR/CHK1-RPA phosphorylation signaling cascade, clear evidence of defect in HR (Fig. 4k, l). Collectively, these results demonstrate that the tandem SER repeats of SAGE1 mediate the direct connection between SAGE1 and CtIP, which recruits SAGE1 to DSB sites to facilitate the end-resection.

SAGE1 recruits and stabilizes the SOSS complex at DSBs for efficient end-resection

To further delve into the regulatory mechanism of end-resection governed by SAGE1, we conducted an immunoprecipitation-mass spectrometry (IP-MS) analysis to identify SAGE1-interacting DDR factors in both *Hs*SPG and SAGE1-positive cancer cells (Supplementary Table S2). Of note, components of two key DNA repair machineries, the SOSS (sensor of ssDNA)[46-50] and the NuA4 (Nucleosome acetyltransferase of H4) complexes[51,52], appeared in the high-confidence hits from both *Hs*SPG and SAGE1- positive cancer cells (Fig. 5a), indicating that the role of SAGE1 in promoting genome stability applies to all SAGE1-expressing cells (Supplementary Fig. S11f–h). Reciprocal IP assay confirmed the interaction between endogenous SAGE1 and the SOSS complex (Fig. 5b). Further biochemical analysis using purified proteins unveiled that SAGE1 could form a stable quaternary complex with SOSS through a direct interaction between the C-terminal domains of both SAGE1 and Integrator complex subunit 3 (INTS3) — the hub of the SOSS complex — on which dock the other two subunits of the complex, NABP1/2 (Nucleic acid binding protein 1/2) and INIP (INTS3 and NABP interacting protein) (Fig. 5c, d; Supplementary Fig. S13h, i). Notably, knockdown of either SAGE1, INTS3, or NABP2 substantially reduced the protein levels of the other two, implying that the interaction between SAGE1 and the SOSS complex mutually enhances the stability of these DDR factors in cells (Supplementary Fig. S13j). Accordant with this notion, IF analysis revealed that ablation of any subunits among SAGE1, INTS3, and NABP2 all compromised their accumulations at DSBs (Fig. 5e, f; Supplementary Fig. S13k). The SOSS complex plays an important role in HR-mediated DSB repair, where NABP2 is involved in the stimulation of end-resection by EXO1[46,53-55]. Given the close interaction between SAGE1 and the SOSS complex and the quick recruitment of SAGE1 to DSBs upon DNA damage (Figs. 3b, 5c), we hypothesized that SAGE1 might facilitate targeting the SOSS complex to DSBs, and thereupon bolster the end-resection. Consistent with this idea, introducing human SAGE1 into MEF cells greatly enhanced the recruitment of INTS3 and NABP2 to the DNA damage sites (Fig. 5g–j; Supplementary Fig. S13l–n). In contrast, SAGE1$_{\Delta\mathrm{SER}}$ mutant did not influence the positioning of INTS3 and NABP2 at DSBs (Fig. 5g–j). Moreover, although SAGE1$_{\mathrm{SER}}$ itself could be quickly recruited to the damage sites, it had no detectable impact on the dynamic targeting of INTS3 and NABP2 to DSBs due to the lack of the C-terminal INTS3-binding domain (Fig. 5g–j). Notably, ectopically expressed SAGE1 failed to enhance the recruitment of exogenous NABP2 to damage sites in MEF cells in the absence of INTS3 overexpression (Supplementary Fig. S13o). Taken together, these results demonstrated that both the SAGE1–CtIP and the SAGE1–INTS3 interactions are prerequisites for rapid, efficient SOSS recruitment and subsequent end-resection at DSBs. Thus, we conclude that the newly evolved tandem SER repeats cooperating with the ancestral INTS3-binding motif endow SAGE1 with an uncharacterized ability to establish a physical link between CtIP and the SOSS complex (Figs. 4d, 5c), enabling efficient recruitment of the SOSS complex to enhance the process of end-resection at DSB sites.

Tandem SERs recruit the NuA4 complex to suppress NHEJ and activate ATM at DSBs

The NuA4 histone acetyltransferase complex plays a well-established role in DSB repair by favoring HR and antagonizing the NHEJ machinery[56-60]. Our IP-MS analysis, which detected multiple NuA4 components as SAGE1 interactors, prompted a mechanistic model in which SAGE1 mediates the recruitment of the NuA4 complex to DSB sites, thereby suppressing NHEJ and channeling repair toward HR (Fig. 5a). To test this hypothesis, we first confirmed the interactions of SAGE1 with the NuA4 complex using co-IP experiments, and demonstrated that the tandem SERs (primarily SER$_{14}$) of SAGE1 mediate a direct interaction with NuA4 component RUVBL1 (Fig. 6a, b; Supplementary Fig. S14a). Glycerol gradient centrifugation analysis of SAGE1 immunoprecipitated sample from Expi293F cells unveiled co-sedimentation of Flag-tagged SAGE1 with endogenous NuA4 complex, further corroborating their association (Supplementary Fig. S14b). In addition, *in vitro* reconstitution using purified proteins showed that SAGE1$_{\mathrm{SER11-14}}$, RUVBL1, RUVBL2, and the ATPase domain of EP400 (EP400$_{\mathrm{ATPase}}$, residues 1,085–1,450 + 1,738–2,046) can assemble into a stable complex (Fig. 6c; Supplementary Fig. S14c, d). Together, our biochemical data strongly support the notion that the evolution of the tandem SERs enabled SAGE1 to acquire a novel interaction with the NuA4

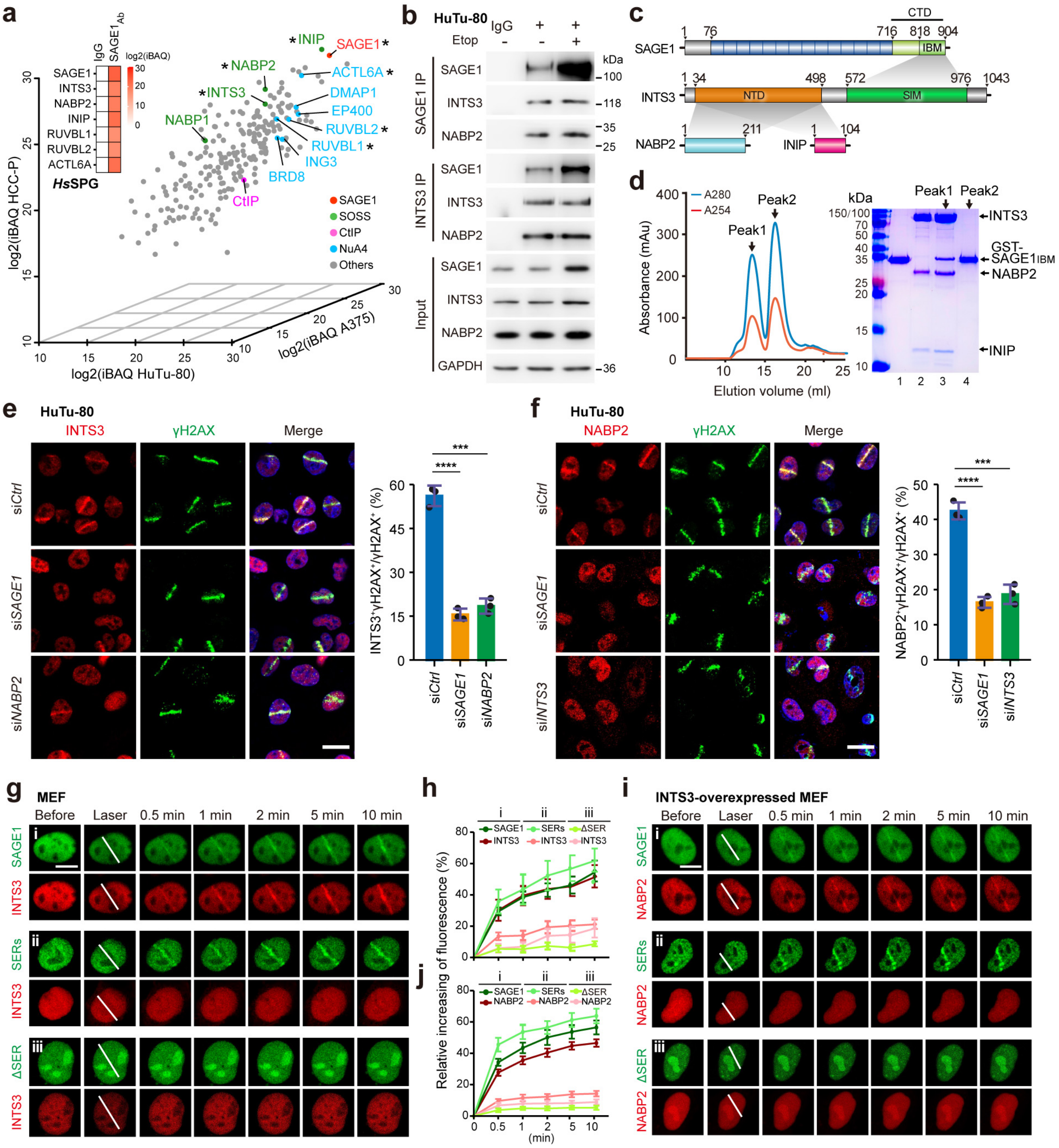

Fig. 5 SAGE1 recruits and stabilizes the SOSS complex at DSBs. a Identification of SAGE1-interacting proteins by IP-MS. The scatterplot shows SAGE1-interacting proteins identified in independent IP assays conducted with various cancer cell lines and *Hs*SPG as indicated. Enriched bait protein SAGE1, along with co-enriched proteins, CtIP, SOSS and NuA4 components, are marked with color-coded dots and annotated for clarity. The inset highlights the specific enrichments of SAGE1-interacting factors (indicated by * in the scatterplot) in *Hs*SPG. **b** Reciprocal IP of SAGE1 and SOSS in HuTu-80 cells with or without etoposide treatment. **c** Schematic diagram of the domain organizations of SAGE1 and the SOSS complex highlighting the interacting domains. **d** Purification of the GST-SAGE1$_{\mathrm{IBM}}$–SOSS complex. Left: size exclusion chromatographic profile of the SOSS complex with GST-SAGE1$_{\mathrm{IBM}}$. 87-residue fragment of SAGE1 (residues 818–904), hereafter referred to as the INTS3-binding motif of SAGE1 (SAGE1$_{\mathrm{IBM}}$). Right: Coomassie-stained SDS-PAGE of the corresponding peaks in the profile. Lane 1: GST-SAGE1$_{\mathrm{IBM}}$, Lane 2: the SOSS complex, Lane 3: the SOSS complex with GST-SAGE1$_{\mathrm{IBM}}$ of Peak 1, Lane 4: GST-SAGE1$_{\mathrm{IBM}}$ of Peak 2. **e** Representative IF images of INTS3 and γH2AX in laser-microirradiated siCtrl, si*SAGE1*, and si*NABP2* HuTu-80 cells, with co-localization quantified on the right. Scale bar, 20 µm. $n = 3$ independent replicates with at least 100 cells per condition were analyzed. **f** Representative IF images of NABP2 and γH2AX in laser-microirradiated siCtrl, si*SAGE1*, and si*INTS3* HuTu-80 cells, with co-localization quantified on the right. Scale bar, 20 µm. $n = 3$ independent replicates with at least 100 cells per condition were analyzed. **g** MEF cells were co-transfected with mCherry-INTS3 and EGFP-SAGE1 (i), EGFP-SAGE1$_{\mathrm{SER}}$ (ii), or EGFP-SAGE1$_{\Delta\mathrm{SER}}$ (iii), then subjected to laser micro-irradiation and real-time recruitment assays. White lines indicate laser paths. Scale bar, 10 µm. **h** The quantification of fluorescence intensity was shown in panel (**g**). $n = 10$ cells were analyzed. **i** INTS3-overexpressed MEFs were co-transfected with mCherry-NABP2 and EGFP-SAGE1 (i), EGFP-SAGE1$_{\mathrm{SER}}$ (ii), or EGFP-SAGE1$_{\Delta\mathrm{SER}}$ (iii), then subjected to laser micro-irradiation and real-time recruitment assays. White lines indicate laser paths. Scale bar, 10 µm. **j** The quantification of fluorescence intensity shown in panel (**i**). $n = 10$ cells were analyzed. For all experiments, data are shown as mean ± SD. Significance was determined with two-tailed Student's *t*-test. $^{***}P < 0.001$, $^{****}P < 0.0001$.

complex in simians.

Consistent with a functional role in recruitment, *SAGE1* knockdown significantly reduced the accumulation of RUVBL1 and TIP60 (the catalytic subunit of NuA4) at DSBs (Fig. 6d–g; Supplementary Fig. S14e). This defect was efficiently rescued by re-expression of WT SAGE1, but not by SAGE1$_{\Delta\mathrm{SER}}$, underscoring the critical role of the SERs in recruiting NuA4 to damage sites (Fig. 6d–g). In contrast, depletion of RUVBL1 or

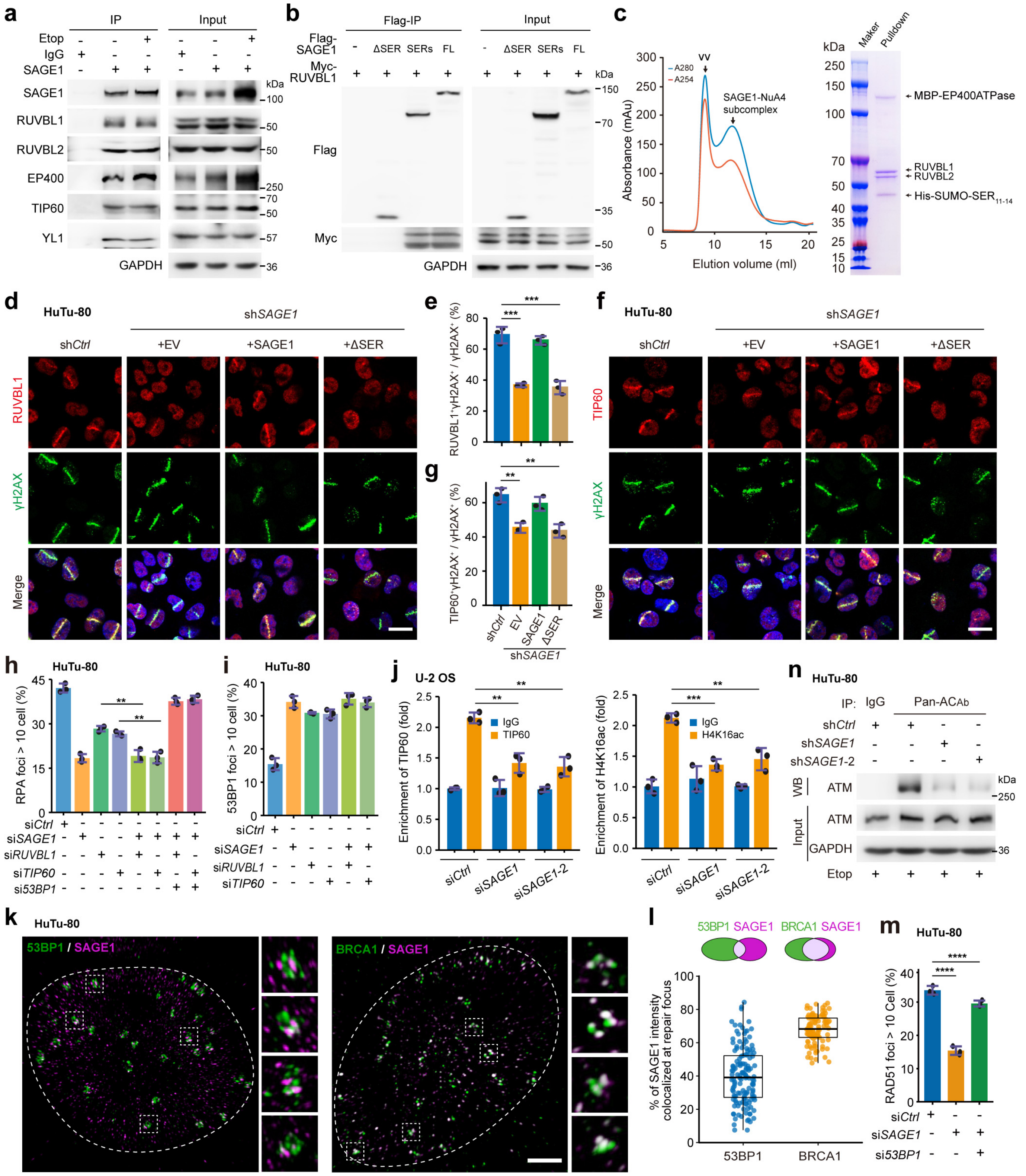

Fig. 6 Tandem SAGE1 SERs recruit the NuA4 complex to suppress NHEJ and activate ATM at DSBs. a HuTu-80 cell lysates with or without etoposide treatment were immunoprecipitated with anti-SAGE1 antibody, and then analyzed by western blot. **b** Co-IP experiments in HEK293T cells co-transfected with plasmids expressing Myc-RUVBL1 and various Flag-SAGE1 truncations. **c** Purification of the SAGE1$_{SER11-14}$–NuA4 submodule complex. Size exclusion chromatographic profile of the SAGE1$_{SER11-14}$–NuA4 submodule complex (left). The void volume peak (vv) and the SAGE1$_{SER11-14}$–NuA4 submodule complex peak are labeled. Coomassie-stained SDS-PAGE of the corresponding peaks in the profile (right). **d, e** Representative IF images of RUVBL1 and γH2AX in laser-microirradiated shCtrl, sh*SAGE1* + EV, sh*SAGE1* + SAGE1, and sh*SAGE1* + ΔSER HuTu-80 cells (**d**), with co-localization quantified on panel (**e**). Scale bar, 20 μm. *n* = 3 independent replicates with at least 100 cells per condition. **f, g** Representative IF images of TIP60 and γH2AX in laser-microirradiated shCtrl, sh*SAGE1* + EV, sh*SAGE1* + SAGE1, and sh*SAGE1* + ΔSER HuTu-80 cells (**f**), with co-localization quantified on panel (**g**). Scale bar, 20 μm. *n* = 3 independent replicates with at least 100 cells per condition. **h** Quantification of the percentage of HuTu-80 cells with more than 10 RPA foci after etoposide treatment in different siRNA transfected conditions. *n* = 3 independent replicates with at least 100 cells per condition. **i** Quantification of the percentage of HuTu-80 cells with more than 10 53BP1 foci after etoposide treatment in different siRNA transfected conditions. *n* = 3 independent replicates with at least 100 cells per condition. **j** ChIP-qPCR performed with TIP60 and H4K16ac antibodies in the presence of I-SceI induced DSBs in DR-U-2 OS-siCtrl or -si*SAGE1* cells. *n* = 3 independent replicates. **k** Representative super-resolution SIM images reveal the non-overlapped juxtaposition of SAGE1

and 53BP1, and the colocalization of SAGE1 and BRCA1 at etoposide induced DSBs in HuTu-80 cells treated with etoposide (10 μM) for 4 h and released for 2 h. White box areas were enlarged on the right of the images. Scale bar, 2 μm. **l** The quantification of panel (**k**). **m** Quantification of the percentage of HuTu-80 cells with more than 10 RAD51 foci after etoposide treatment in different siRNA transfected conditions. *n* = 3 independent replicates with at least 100 cells per condition. **n** Cell lysates from sh*Ctrl* and sh*SAGE1* HuTu-80 cells treated with etoposide were immunoprecipitated with anti-Pan Acetyl-Lysine antibody (Pan-ACab), then analyzed by western blot. For all experiments, data are shown as mean ± SD. Significance was determined with two-tailed Student's *t*-test. $^{**}P < 0.01$, $^{***}P < 0.001$, $^{****}P < 0.0001$.

TIP60 did not impair SAGE1 recruitment to DSBs, indicating that SAGE1 acts upstream of the NuA4 complex in the DDR hierarchy (Supplementary Fig. S14f, g). Epistasis analysis further revealed that the severity of impaired RPA recruitment and enhanced 53BP1 accumulation in SAGE1-depleted cells was comparable to that in SAGE1-RUVBL1 or SAGE1-TIP60 double-knockdown cells (Fig. 6h, i; Supplementary Fig. S14h), confirming that SAGE1 and the NuA4 complex operate within the same HR-promoting pathway.

TIP60 acetylates histone H4 at lysine 16 (H4K16ac), a modification that antagonizes 53BP1 binding to H4K20me2 at DSBs[61]. SAGE1 depletion reduced both TIP60 recruitment and H4K16ac levels near damage sites (Fig. 6j). Conversely, ectopic expression of human SAGE1 in MEF cells markedly enhanced the recruitment of RUVBL1 and H4K16ac at DSBs (Supplementary Fig. S14i). These data are consistent with an HR–to–NHEJ switch upon SAGE1 loss (Fig. 3f). Because 53BP1 recruitment is largely mediated by RNF168-dependent ubiquitination of H2A histones[62], we asked whether SAGE1 affects this event. IF data showed that SAGE1 depletion did not alter RNF168 recruitment to etoposide-induced damage sites (Supplementary Fig. S14j). Western blot analysis further confirmed that SAGE1 knockdown had no detectable effect on global ubiquitination or on H2AK119ub levels (Supplementary Fig. S14k, l). Collectively, these results demonstrate that SAGE1-mediated suppression of 53BP1 is independent of the RNF168 ubiquitin-signaling cascade, and instead operates through the NuA4/TIP60-dependent acetylation of H4K16.

To further illustrate SAGE1-mediated suppression of 53BP1 localization to DSBs, we performed IF analysis using high-resolution Structured Illumination Microscopy (SIM). SIM images clearly showed that SAGE1 preferentially co-localizes with BRCA1, rather than 53BP1, at the damage sites (Fig. 6k, l). This finding demonstrates that SAGE1 suppresses 53BP1 localization to DSBs, indicating that the inefficient resection at DSBs in SAGE1-depleted cells could be due to the unchecked inhibitory effect of 53BP1. To test this idea, we depleted 53BP1 in SAGE1-knockdown cells and evaluated RAD51 localization upon etoposide treatment. Indeed, depleting 53BP1 rescued the resection defect caused by SAGE1 loss, restoring the RAD51 signal at DSBs back to the level comparable to that in control cells (Fig. 6m; Supplementary Fig. S14m). Notably, depletion of 53BP1 also rescued the defect in RPA foci formation in SAGE1–RUVBL1 and SAGE1–TIP60 double-knockdown cells (Fig. 6h), further demonstrating the epistasis relationship of SAGE1 and the NuA4 complex in the HR repair pathway. Collectively, we conclude that SAGE1 recruits the NuA4 acetyltransferase activity to the damage sites, which restricts the access of 53BP1 to DSBs by the acetylation on H4K16.

Besides histone H4, another important, non-histone substrate for TIP60 acetyltransferase activity is the protein kinase ATM (ataxia telangiectasia mutated) that plays a crucial role in the detection and repair of DSBs through the phosphorylation of multiple proteins involved in cell-cycle checkpoints and DNA repair[63]. Given that TIP60-dependent acetylation of ATM represents a key step in the activation of ATM's kinase activity[63], we investigated whether the SAGE1-mediated TIP60 recruitment to DSBs also contributes to ATM activation. Indeed, knockdown of *SAGE1* abolished the acetylation of ATM, which consequently led to a marked reduction of the ATM/CHK2 phosphorylation signaling cascade, underscoring the critical role of SAGE1 in ATM activation during the DDR process (Fig. 6n; Supplementary Fig. S14n, o). In aggregate, these results depict a mechanistic picture of how $\text{SAGE1}_{\text{SER}}$-dependent recruitment of the NuA4 complex suppresses NHEJ and activates ATM via TIP60 acetyltransferase activity at the DNA damage sites.

DISCUSSION

The ability to faithfully replicate and repair DNA is a fundamental trait critical for the survival and reproduction of organisms. Consequently, various repair mechanisms have evolved to ensure the integrity of genetic information, with sensory and effector components emerging early in evolution, followed by the development of regulatory elements that fine-tune these processes (Supplementary Table S3)[1,2,12]. By integrating evidence from multiple experimental systems involving primary SPG cells from mice, macaques, and humans, along with *in vivo* analyses in macaques, mice, and *Drosophila*, our current work demonstrates that *SAGE1* — an X-linked, simian-specific gene enriched in SPG — is a recently evolved yet uncharacterized DDR regulator, which plays a pivotal role in preserving simian germline genome integrity. We propose that the novel function of SAGE1 represents an 'u pgradation' to the existing DDR landscape by introducing an additional layer of regulation (Fig. 7; Supplementary Table S3).

To ensure the precise delivery of intact genetic material to the next generation, DNA proofreading and repair are critically required for SPG cells, which could evolutionarily drive the positive selection for the emergence of novel genes that enhance HR-mediated DDR capabilities. By offering a vivid example of this hypothesis, our findings demonstrate that the emergence of SAGE1 facilitates enhanced germline genome stability in simians. SAGE1 evolved a specialized, yet essential function in coordinating the choice of the HR pathway for efficient DDR. With the newly evolved tandem SERs, SAGE1 acquires the ability to interact with CtIP as well as the SOSS and NuA4 complexes, tilting the balance in favor of the error-free HR pathway to promote germline genome stability (Fig. 7).

Our data suggest that the evolution of SAGE1 did not create a fundamentally new repair pathway but rather introduced an optimized regulatory module that accelerates and refines the conserved HR machinery. This is supported by our finding that mouse cells, which naturally lack SAGE1, could be fully competent to respond to this upgraded regulatory input — ectopic SAGE1 expression enhances HR factor recruitment and chromatin remodeling (e.g., SOSS and H4K16ac enrichment) at DSBs (Figs. 5g–j, 6j; Supplementary Fig. S14i). Thus, SAGE1 likely represents a lineage-specific 'turbocharger' for the core HR apparatus, providing simians with a selective advantage in maintaining germline fidelity.

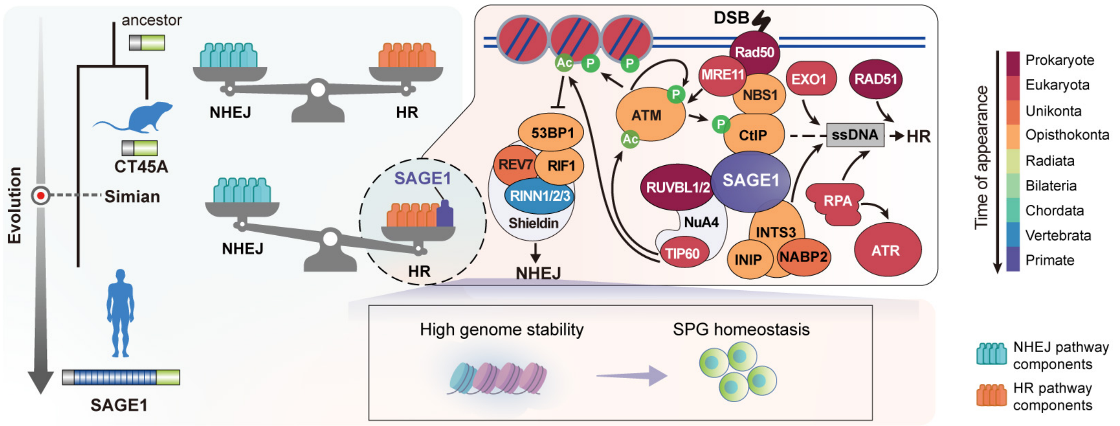

Fig. 7 A proposed model of SAGE1's role in simian germline genome integrity. *SAGE1* is a recently evolved DDR-related gene unique to simians. Upon DSBs, SAGE1 is recruited to DSB sites via the MRN–CtIP complex, facilitating SOSS complex stability and promoting resection at DSBs, which enhances RPA and RAD51 association. Moreover, SAGE1 also recruits the NuA4 complex, triggering TIP60-mediated acetylation of H4K16. Acetylated H4K16 inhibits 53BP1 localization, suppressing the NHEJ pathway. Collectively, the action of SAGE1 at DSBs enhances the HR pathway while reducing the NHEJ activity, promoting simian germline genome integrity.

Owing to the restricted expression profile of SAGE1, the DDR network of non-germline cells likely remains unaffected by this novel gene, allowing germ cells to gain augmented DNA repair capabilities without interfering with normal somatic cell physiology. Given the connection between genome integrity in SPG and germline mutations[19,20,25], it is tempting to speculate that the evolution of SAGE1 might play a key role in contributing to the lower germline mutation rates observed in simians. SAGE1's evolutionary significance in this context remains to be further explored.

Intriguingly, transcriptomic expression profiles of the human ovary from 4 weeks post-conception (WPC) to adulthood revealed that SAGE1 displays an expression peak in fetal ovary at about 9–16 WPC, matching the timing when the oogonia undergo the only round of amplification during the entire female lifetime (Supplementary Fig. S15a, b)[64,65]. Our IF analysis of 13-WPC human fetal ovarian tissues showed a clear co-expression of SAGE1 with DDX4 (oogonia marker) (Supplementary Fig. S15c). This unique SAGE1 expression pattern in mitotically active germline precursors of both sexes strongly suggests that SAGE1's function in promoting genome stability is likely conserved across male and female gametogenesis. Future studies will be needed to elucidate the common mechanism of how SAGE1 regulates both male and female germ cell development.

DNA repair tools must be tightly regulated in a temporal, spatial fashion because each in its own right can wreak havoc on cellular or organismal homeostasis if dysregulated or aberrantly activated at the wrong time or location[2,66,67]. We show here that SAGE1 functions as a potent 'HR-enhancing module' whose expression is normally confined to the germline (Figs. 1g, 2c; Supplementary Fig. S3a–c). However, when aberrantly reactivated in cancer cells, this germline-specific program can be co-opted to bolster DNA repair in malignant somatic cells. This hijacking of SAGE1's HR-promoting capacity may help cancer cells maintain their corrupted genome and contribute to therapy resistance. Consequently, targeting SAGE1, particularly in combination with DNA-damaging agents, could represent a novel therapeutic strategy to selectively sensitize SAGE1-positive tumors.

MATERIALS AND METHODS

Human testis and ovary samples collection

Testes were collected from patients undergoing bilateral orchidectomy as part of their management for prostate cancer, at the Urology Department, Shanghai Ninth People's Hospital (ethics approval number: SH9H-2019-T279-5). The patients were fully informed before signing consent to donate excess tissue for research. All patients fathered at least one child, and had no history of chemotherapy, radiotherapy, or hormonal treatments prior to the surgery. De-identified formalin-fixed, paraffin-embedded (FFPE) ovarian tissues from the aborted embryo were provided by the Department of Obstetrics and Gynecology, Shanghai Ninth People's Hospital (ethics approval number: SH9H-2020-T389-4).

Isolation, magnetic-activated cell sorting (MACS) and culture of SPG from human testes

The complete and normal spermatogenesis of all testis tissues used in our experiments was confirmed by histological evaluation with Hematoxylin and Eosin staining. Once collected, the testis samples were transported to the research laboratory on ice in tissue storage solution (Miltenyi #130-100-008), and processed within 1 h after removal by surgery. Testicular cells were isolated using a two-step enzymatic digestion protocol described previously[33,68]. Briefly, testicular tissues were digested with collagenase type IV (Sigma Aldrich #C5138-500MG) for 5 min at 37 °C with gentle agitation (180 rpm), then shaken vigorously and incubated for another 3 min. The tubules were sedimented by centrifugation at 200× *g* for 5 min and washed with Hank's Balanced Salt Solution (HBSS) before digestion with 4.5 mL 0.25% trypsin/ethylenediaminetetraacetic acid (EDTA, Invitrogen #25300054) and 4 kU DNase I (Sigma Aldrich #D4527-500ku). The suspension was triturated vigorously three to five times and incubated at 37 °C for 5 min. The process was repeated in 5-min increments for up to 20 min in total. The digestion was stopped by adding 10% FBS (Gibco #10082147). Testicular cells were obtained by filtering through 100-, 70-, and 40-μm nylon cell strainers (Corning #352360, 35250 and 352340) under sterile conditions. Somatic cells were allowed to adhere overnight, and the supernatant containing SPGs was then harvested. Next, dead cells were removed using the Dead Cell Removal Kit (Miltenyi #130-090-101), and live cells were collected in the flow-through in 1 mL of binding buffer (Miltenyi #130-091-221). Then c-KIT$^+$ spermatogonia were purified using the MACS system. Briefly, testicular cell suspensions were incubated with CD117 microbeads (Miltenyi #130-091-332) for 15 min at 4 °C. Following microbead binding, cells were re-suspended and run through LS columns (Miltenyi #130-042-401) placed in a magnetic field. The columns were rinsed three times with running buffer before being removed from the magnetic field. MACS running/separation buffer (Miltenyi #130-091-221) was then applied to the column before magnetically-labeled cells were flushed out by firmly pushing the plunger into the column. Cells were subsequently centrifuged and re-suspended to the desired concentration.

For short-term culture, human SPG were maintained in StemPro-34 medium (Gibco #10639011), containing 20 ng mL^{-1} recombinant human EGF (R&D #236-EG), 50 ng mL^{-1} GDNF (R&D Systems #212-GD), 10 ng mL^{-1} LIF (R&D #7734-LF), 10 ng mL^{-1} FGF2 (Peprotech #100-18B), 1× ITS-G (Gibco #41400-045), and 1% FBS (Gibco #10091148) on laminin-coated cell culture dish.

Crab-eating macaque testis samples collection

Testes were collected from adult nulliparous crab-eating macaques (*Macaca fascicularis*) with complete health records, at NHP Research Animal Facility of the PharmaLegacy CRO, which is fully accredited by the Association for Assessment and Accreditation of Laboratory Animal Care, after ethics approval from the IACUC of this facility (protocol number: PL22-0280-C-1).

Isolation, MACS and culture of SPG from crab-eating macaque testes

Testis tissues were transported to the research laboratory on ice in tissue storage solution (Miltenyi #130-100-008) within 1 h after removal by surgery. Spermatogonia were isolated and purified using the same protocol as human testicular cells, except for reducing the trypsin-digestion time to 10 min.

For short-term culture, macaque SPG were maintained in StemPro-34 medium (Gibco #10639011), containing 20 ng mL^{-1} recombinant human EGF (R&D #236-EG), 50 ng mL^{-1} GDNF (R&D Systems #212-GD), 10 ng mL^{-1} LIF (R&D #7734-LF), 10 ng mL^{-1} FGF2 (Peprotech #100-18B), 1×ITS-G (Gibco #41400-045), and 1% FBS (Gibco #10091148) on laminin-coated cell culture dish.

In vivo experiments of crab-eating macaque

The study used adult nulliparous cynomolgus macaques (*M. fascicularis*, $n = 2$; age, 5–6 years) with complete health records for *in vivo* RNA interference experiments. All procedures were performed at NHP Research Animal Facility of the PharmaLegacy CRO, which is fully accredited by the Association for Assessment and Accreditation of Laboratory Animal Care, after ethics approval from the IACUC of this facility (protocol number: PL22-0280-C-1). Animals were housed individually in standard non-human primate cages, received standard primate feed as well as fresh fruit and enrichment daily, and had continual access to water. Temperature (19–24 °C), humidity (45–60%) and light (approximately 323 lux) were monitored and maintained within recommended limits, the light/dark cycle was maintained at 12-h split. Environmental enrichment was provided. Animals were observed twice daily by the veterinary staff for signs of clinical illness.

Operation was performed on deeply anesthetized animals [ketamine, 10 mg/kg; xylazine 0.5 mg/kg, intramuscular injection (IM)]. Under aseptic conditions, a 0.5–1cm incision was made in the top and bottom scrotum quadrant to expose tunica albuginea. 2 mL of 2×10^{13} VG of AAV9 was slowly injected by multipoint interstitial injections using a 26-gauge injection needle. All procedures were performed using aseptic techniques, and color flow Doppler was utilized to avoid perforation of blood vessels. The incision was sutured, and postoperative care was provided according to IACUC-approved clinical procedures, including the use of analgesia (ketoprofen, 5 mg/kg, IM for 3 days). The animals were euthanized 4 months after AAV9 injection, and bilateral testicles were isolated and weighed. A portion of testicular tissue was used for organotypic testis culture, other parts were prepared as formalin-fixed paraffin tissue blocks for subsequent experiments.

Ex vivo assays on macaque testis

Macaque testicular tissues were cut into small blocks and fixed on the specimen holder of VT1200 vibrating-blade microtome, sectioned at a thickness of 400 μm by keeping vibration amplitude at 2.85 mm and speed at 0.3 mm/s. Slices were gently transferred into DMEM medium (containing 15% FBS and 1% PS) and stored for at least 30 min to recover from the slicing procedure. Afterwards, the slices were incubated with 50 μM cisplatin in a 37 °C incubator for 2 h and then recovered for 4 h. After washing, slides were embedded in paraffin for immunohistochemical analysis.

Knock-in mouse line generation and irradiation treatment

The *Rosa26-SAGE1* knock-in mouse line was generated by the CRISPR/Cas9 technology. To generate a *SAGE1*-floxed Rosa26 line, we inserted a *SAGE1* transgene expression cassette into the Rosa26 locus. The donor vector consists of a 3× FLAG-tagged SAGE1, linked via a self-cleaving P2A peptide to an enhanced green fluorescent protein (EGFP). The transgene is driven by the ubiquitous CAG promoter and is interrupted by a loxP-stop (2× polyA signal)-loxP cassette to allow inducible SAGE1 expression by the Cre recombinase. Resulting founder male mice were mated to WT C57BL/6J female mice to obtain heterozygous *SAGE1*-floxed mice. Progeny were screened by PCR for germ line transmission of the targeted alleles. For conditional knock-in of *SAGE1* in advanced germ cells, $SAGE1^{flox/+}$ were then bred with germ cell-specific Cre-expressing mice including *Vasa-Cre* male mouse line (Jackson Laboratory, Bar Harbor, Maine, USA) to generate germ cell-specific *SAGE1* knock-in mice. All mice described above were maintained on the C57BL/6J background. All of the primers for PCR genotyping were listed in Supplementary Table S4. The *Vasa-Cre* and $SAGE1^{flox/+}$; *Vasa-Cre* mice were used in this study. 5-week old mice were irradiated with 1 Gy X-irradiation at a dose rate of 1.28 Gy/min using a RAD SOURCE RS-2000 Pro Biological Irradiator followed by recovery for 5 h. After recovery, testes were dissected and stained.

Isolation and culture of SPG from mouse testes

Testes were collected from male C57Bl/6J mice at postnatal days (P) 5–7 at Animal Facility of the Shanghai Ninth People's Hospital (ethics approval number: SH9H-2023-A912-1), and then decapsulated and minced in ice-cold Dulbecco's Modified Eagle Medium (DMEM, Gibco #11960044). SPG were isolated using a two-step enzymatic digestion protocol described previously[69,70]. First, Leydig cells, peritubular myoid cells, and other interstitial cells were eliminated by enzymatic digestion with 1 mg mL^{-1} collagenase IV and 10 μg mL^{-1} DNase I in Dulbecco's Modified Eagle Medium/Nutrient Mixture F-12 (DMEM/F12, Gibco #11320033) at 35 °C for 10 min and extensively washed with PBS to only obtain the seminiferous tubules. Germ cells and Sertoli cells were isolated by a second enzymatic digestion using 0.25% trypsin/EDTA under the same conditions. The digestion was stopped by adding 10% FBS and cells were filtered through 40-μm filters. For enrichment of SPG, cell suspensions were subjected to differential plating to remove fibroblasts and Sertoli cells. Briefly, cells were seeded at a concentration of 4×10^5 mL^{-1} in 6-cm dishes (Corning #3261) coated with 0.2% (w/v) gelatin in high glucose DMEM supplemented with 10% FBS and 1% penicillin-streptomycin, and incubated in a 5% CO_2 atmosphere at 37 °C with 85% relative humidity. After 2 h, floating cells were transferred to new dishes for overnight incubation under the same conditions. The next morning, floating germ cells were collected and resuspended in StemPro-34 based medium for further experiments.

Mouse SPG were cultured for short-term in StemPro-34 medium, containing 25 ng mL^{-1} recombinant human EGF (Peprotech #31509), 15 ng mL^{-1} GDNF (Peprotech #A1838), 10 ng mL^{-1} LIF (Peprotech #25002), 10 ng mL^{-1} FGF2 (Peprotech #45033), 20 ng mL^{-1} IGF1 (Peprotech #25019), and 1% FBS on laminin-coated cell culture dish.

Drosophila genetics, and irradiation treatment

Full-length human *SAGE1* fragment was cloned into the pUAST vector tagged with GFP, and transgenic *UAS-SAGE1-GFP Drosophila* were generated using germline transformation techniques. Then, *Drosophila* strain overexpressing human SAGE1 in the germline stem cells and spermatogonia was obtained by crossing *UAS-SAGE1-GFP* flies to *Nanos-Gal4 Drosophila*. The stable *UAS-SAGE1-GFP; Nanos-Gal4 Drosophila* line and w^{1118} as WT control were used in this study. 3/4-day-old flies were irradiated with 10 Gy X-irradiation at a dose rate of 1.28 Gy/min using a RAD SOURCE RS-2000 Pro Biological Irradiator followed by recovery for 3 or 6 h at 25 °C. After recovery, testes were dissected and stained as described in the IF Procedure. *Nanos-Gal4* (BS64188, y[1]w[*]; P{w[+mC]=GAL4::VP16-nanos.UTR}1C, P{w[+mC]=UAS-FLP.D}JD2/TM6) and w^{1118} were obtained from the Bloomington Drosophila Stock Center (BDSC). All *Drosophila* strains were raised at 25 °C with a 12 h dark/light cycle.

Single-cell RNA-seq library construction and data processing

Isolated SPG were collected and resuspended with PBS. Single cells were captured by the 10× Genomics Chromium Single Cell 3′ Solution. scRNA-seq library was conducted by Shanghai Xu Ran Biotechnology and prepared with Chromium Next GEM Single Cell 3′ Kit v3.1 (10× Genomics #PN-1000268) following the manufacturer's instruction. The libraries were subjected to high throughput sequencing on Illumina Nova Seq 6000 platform, and 150-bp paired-end reads were generated. The paired-end FASTQ files from the SPG 10× library were aligned to the corresponding reference genome: GRCh38 for human, Crab_Macaque6 for crab-eating macaque, and mm10 for mouse using cellranger along with filtering, barcode counting, and UMI counting. The aligned matrix was then loaded in a Seurat (v4.1.0) for subsequent analysis. Low-quality cells, doublets and potential dead cells were removed according to the percentage of mitochondrial genes and the number of genes and UMIs expressed in each cell (nFeature_RNA > 500 & nFeature_RNA < 10000 & percent.mt < 15 & percent.ribo < 50). Clean count matrices were normalized, dimension reduced, and visualized using Seurat (v4.1.0). Cell-type annotation was determined based on both well-known marker genes for each testicular cell type and the automate annotation pipeline of SingleR with known cell types of the corresponding publicly available scRNA-Seq data from the unsorted testis of human[33], crab-eating macaque[34], and mouse[71].

Cell lines

U-2 OS, A375, and HEK293T cells were obtained from ATCC and cultured in DMEM (Gibco #10569044) with 10% FBS (Gibco #A5669701). U-2 OS-DR-GFP, -EJ5-GFP cells were obtained from Dr. Jumin Zhou in Kunming Institute of Zoology, Chinese Academy of Sciences. HuTu-80 cells were obtained from ATCC and cultured in MEM (Gibco #12571063) supplemented with 10% FBS. HCC-P were isolated from a primary sarcomatoid hepatocellular carcinoma and maintained in DMEM supplemented with 15% FBS, 1% Penicillin-Streptomycin (Gibco #15070063), 5 μg mL^{-1} insulin (Sigma #I3536), and 100 ng mL^{-1} hydrocortisone sodium succinate. $Tsc2^{-/-}$, $p53^{-/-}$ MEFs were previously established, and maintained in RPMI1640 (Gibco #21870076) supplemented with 10% FBS and 1× Sodium Pyruvate (Gibco #11360070). All cells were maintained at 37 °C in a humidified incubator with 5% CO_2.

Plasmid construction

To construct the shRNA expression plasmids, shRNA oligos targeting *HsSAGE1* or *MfSAGE1* were designed through an online tool of Ambion siRNA Target Finder. The nucleotide sequences were listed in Supplementary Table S4. The shRNA oligos were synthesized by Sangon Biotech, annealed and inserted into pLKO.1 plasmid. For construction of *Hs*SAGE1, *Mf*SAGE1, *Cj*SAGE1, and *Mmu*CT45A inducible expression plasmids, gene fragments with a Flag-tag were inserted into PBTRE vector which carries *Tet* on promoter. For Co-IP, full-length human SAGE1, $SAGE1_{\Delta SER}$, $SAGE1_{SER}$ were cloned into pEGFP-Flag vector through *Bam*HI and *Xho*I. Full-length and truncated CtIP (residues 1–145, 145–509, 509–790, or 790–897), and full-length RUVBL1 were cloned into pEGFP-Myc vector through *Bam*HI and *Sal*I. pDRGFP, pimEJ5GFP, and pCBASce plasmids were gifts from Dr. Bo Zhao in Kunming Institute of Zoology, Chinese Academy of Sciences. To visualize SAGE1, INTS3, NABP2 in live imaging experiments, SAGE1, $SAGE1_{\Delta SER}$, and $SAGE1_{SER}$ were cloned into plvx-pEGFP-NLS vector by *Bam*HI and *Xho*I. INTS3 and NABP2 were cloned into modified plvx-mcherry-NLS vector. For *Hs*SAGE1, *Hs*$SAGE1_{\Delta SER}$ overexpression plasmids construction, gene fragments were amplified using standard PCR procedure and inserted into the digested Flag-tagged pCDH-CMV-MCS-EF1-copGFP plasmid. All cloned products were confirmed via restriction enzyme digest, Sanger sequencing, and functionally validated via Western blot analysis. The primers used for PCR were listed in Supplementary Table S4.

Lentivirus package

HEK293T cells were seeded in 15-cm dishes for 24 h before transfecting with 16 μg expression vector (pLKO.1 or pCDH), 8 μg pVSVG, and 12 μg DR8.9 plasmid using Lipofectamine 3000 (Thermo Fisher #L3000015). 16 h after transfection, the medium was replaced by fresh DMEM with 10% FBS. The viral supernatants were collected at 48 h and 72 h post-transfection. The viruses were filtered through a 0.45-μm syringe filter and concentrated through an Amicon® Ultra-15

Centrifugal Filter (Millipore #R9EA11841), and stored at −80 °C.

Lentivirus infection

The lentiviral solution was rapidly thawed at room temperature (RT). 1 mL lentivirus, 9 mL SPG medium and 10 μg mL^{-1} polybrene were mixed to prepare the virus solution. 1×10^6 SPG were resuspended with the virus solution and incubated for 24–36 h. Then the media was replaced by 10 mL fresh SPG medium. The cells were sorted with GFP and/or mCherry fluorescence by Flow Cytometry on day 3. Cells were infected with 1 mL lentivirus and 8 μg mL^{-1} polybrene for 12 h, then incubated in fresh medium for 3 days, and subsequently selected with 1 μg mL^{-1} of puromycin (Gibco #A11138-03) for 48 h.

Cell transfection

For pEGFP plasmid transfection, cells were plated one day before transfection, and transfected using Lipofectamine 3000 according to the manufacturer's protocol. For doxycycline (DOX)-inducible expression of Flag-tagged *Hs*SAGE1, *Mf*SAGE1, *Cj*SAGE1, and *Mmu*CT45A in MEF, cells of 6-cm dishes were transfected with 1 μg PBTRE and two helper plasmids (1 μg TET-3G, 1 μg Hyperbase) by Lipofectamine 3000 according to the manufacturer's protocol. For siRNA transfection, cells were plated one day before transfection, and then transfected with Lipofectamine RNAiMAX (Thermo Fisher #13778075) according to the manufacturer's protocol. The siRNAs were designed and synthesized by Genepharma Co., Ltd. (Shanghai, China) and sequences were listed in Supplementary Table S4. Negative control non-targeting siRNA was used in samples where a gene-specific siRNA is not indicated or to bring the total amount of siRNA to equal molar concentrations when comparing samples with one versus two siRNAs.

Recombinant AAV serotype 9 production

The transgene cassette was flanked by AAV-2 inverted terminal repeats with the capsids derived from AAV-9. A recombinant plasmid pAAV-CBG-EGFP-WPRE-H1-Sh*Mf*SAGE1 (target sequence: 5′-CCAAGGAGAAACAAGAACATA-3′) was constructed and co-transfected with pHelper and pAAV-RC into adenovirus-free HEK-293 cells. After 72 h of cultivation, AAV virus particles were collected from the culture medium and cell lysate, purified by density gradient centrifugation, and then the viral titers were determined by quantitative PCR.

Hematoxylin staining and immunohistochemistry (H-IHC)

Hematoxylin staining and IHC were performed on 5 μm formalin-fixed paraffin-embedded sections following dewaxing, rehydration and antigen retrieval in a citrate solution (pH 6.0). After endogenous peroxidase quenching with 3% hydrogen peroxide, sections were incubated with 5% BSA-TBS blocking buffer, diluted primary antibody, and HRP-labeled secondary antibody, then counter-stained with hematoxylin (Sangon Biotech #E607317), dehydrated, and mounted. For accurate morphological characterization of specified nuclei containing SAGE1, slides were first stained with hematoxylin, then subjected to IHC for anti-SAGE1 antibody.

IF staining

Cells were grown on coverslips (ThermoFisher #174950) or glass-bottom dish (Cellvis #D35C4-20-1.5-N) and treated with different DNA damage inducing agents for indicated time periods. Then, cells were fixed with 4% paraformaldehyde (PFA) for 10 min at RT and permeabilized in 0.5% Triton X-100. The cells were washed three times with PBS, blocked with 1% BSA at RT for 1 h, and then incubated with primary antibody (Supplementary Table S5) diluted in blocking buffer at 4 °C overnight. After washing three times with PBS, the cells were incubated with a secondary antibody diluted in blocking buffer at RT for 1 h. DAPI staining was performed after the secondary antibody.

Testes were fixed in 4% PFA, embedded in paraffin and sectioned. Sections were deparaffinized, rehydrated. For IF analysis, sections were boiled in 10 mM sodium citrate buffer (pH 6.0) for 15 min, brought to room temperature, washed in PBS with 0.1% Triton X-100 3 times. Permeabilization of testes was done by incubation with 0.25% Triton-X for 30 min. Testes were then blocked by 3% BSA in PBST for 1 h, before incubation with primary antibody in 3% BSA in PBST at 4˚C overnight. Testes were washed 3 times with PBST and incubated with secondary antibody in 3% BSA in PBST at RT for 2 h. DAPI staining was performed after the secondary antibody. Confocal microscopy was performed on a Zeiss LSM 880 microscope and analyzed by using ImageJ software. For TUNEL labeling, tumor sections were washed and extracted in 0.3% Triton X-100, and labeling procedures followed the manufacturer's instructions (Roche #11684795910).

Laser micro-point irradiation and IF microscopy

Cells were plated onto a glass-bottom dish and allowed to settle for 24 h. Laser micro-point irradiation was then performed under confocal laser scanning microscope (ZEISS LSM 880) using a micro-point laser workstation. Following the laser irradiation, cells were allowed to recover for 1 h, then fixed with 4% PFA for 10 min and subjected to IF staining with corresponding primary antibodies (Supplementary Table S5). For live-cell laser micro-point irradiation, the indicated plasmids were transfected into HuTu-80 or MEF cells 24 h after plating. Laser micro-point irradiation was conducted 24 h after transfection and live-cell imaging was captured using ZEISS LSM 880 equipped with the Live Cell Imaging Workstation. The fluorescence intensity was quantified using ZEISS ZEN-Lite 3.2 software.

High-resolution SIM

Super-resolution imaging was performed on Zeiss Elyra 7 platform with Lattice SIM^2 (Carl Zeiss AG, Germany) equipped with Plan-Apochromat 63×/1.4 Oil DIC M27 lens and PCO.edge 4.2 sCMOS camera. Laser lines with wavelengths of 488 and 561 nm were used for excitation. The images were acquired in 3D lattice SIM with a 32-μm grid and 13 phases in frame fast tracks mode. Raw images were reconstructed using the appropriate tool of Zeiss Zen software (Black version 3.0 with Structured Illumination module) and analyzed with Imaris 9.3.

IP

For each IP, 2×10^7 cells were treated with 10 μM etoposide or DMSO for 4 h, then harvested, washed with cold PBS, and lysed in lysis buffer (50 mM Tris-HCl, pH 7.4, 150 mM NaCl, 1 mM EDTA, 0.05% Triton X-100, 0.1% Sodium deoxycholate, 5% Glycerol, protease inhibitor cocktail (MedChemExpress #HY-K0010)). The lysate was incubated on ice for 10 min and sonicated by Bioruptor Plus (Diagenode) (40% amplitude/power, ON 3 sec-OFF 3 sec) for 30 cycles. The lysates were centrifuged at maximum speed for 10 min to remove debris. 1 mL of supernatants was incubated with 2–5 μg corresponding antibodies (Supplementary Table S5) and 20 μL Dyna-Green Protein A/G Beads (Thermo Fisher #80105G) overnight at 4 °C with rocking. Then beads were washed three times with lysis buffer and eluted in 0.2 M glycine (pH 2.2) for liquid chromatography tandem mass spectrometry analysis, or eluted in SDS loading buffer by boiling at 95 °C for 5 min for Western blot analysis.

Chromatin fraction extraction

HuTu-80 cells were treated with 10 μM etoposide or 4 mM HU for 4 h, then harvested, washed with cold PBS 3 times and resuspended in the lysis buffer (20 mM HEPES-KOH, pH 7.5, 1 mM EDTA, 10 mM KCl, 0.05% NP-40, 1 mM DTT, protease inhibitor, phosphatase inhibitor mix) for 20 min on ice. The chromatin was obtained by centrifugation and resuspended in the chromatin extract buffer (20 mM HEPES-KOH, pH 7.5, 1 mM EDTA, 600 mM KCl, 1% Triton X-100, 25% glycerol, 1 mM DTT, protease inhibitor cocktail) for 30 min. The supernatant was collected by centrifugation for Western blot analysis.

Co-IP

HEK293T cells were co-transfected with the indicated plasmid constructs using Lipofectamine 3000. 48 h after transfection, the cells were harvested, washed once with PBS, and lysed for 15 min on ice with 500 μL Lysis Buffer (50 mM Tris-HCl, pH 7.4, 150 mM NaCl, 1% Triton X-100, 0.05% SDS, 1 mM EDTA, 1 mM DTT, 1 mM PMSF, and protease inhibitor cocktail). Cell lysates were centrifuged and supernatants were precleared and immunoprecipitated with anti-His antibody (Proteintech #66005-1-Ig), or anti-FLAG antibody (Proteintech #20543-1-AP) at 4 °C overnight with rocking. Protein A/G agarose beads (Millipore #LSKMAGAG02) were added and rotated for 2 h. Precipitates were then washed with lysis buffer and subjected to western blot analysis.

Western blotting

Total proteins were extracted with RIPA buffer (Beyotime #P0013B), subjected to SDS-PAGE separation, and then blotted onto PVDF membranes (Millipore # IPVH00010). The blots were incubated in blocking buffer (5% fat-free milk in PBS buffer supplemented with 0.05% Tween-20) at RT for 1 h and incubated with primary antibodies (Supplementary Table S5) in blocking buffer at 4 °C overnight. Blots were then washed and incubated in HRP-labeled secondary antibodies at RT for 1 h. After washing, blots were developed with ECL Prime Western Blotting System (GE Healthcare RPN2232). The ImageJ software was used to quantitate the immunoblotting data.

Cell Synchronization

HuTu-80 cells were cultured in 6-cm dishes at 40% confluency (1.3 × 10^5 cells). Cells were synchronized by double thymidine (TdR) blocking using a high concentration of TdR (Sigma-Aldrich #50-89-5). Specifically, cells were cultured in medium supplemented with 2 mM TdR for 17 h, and switched to TdR-free medium for 9 h. Cells were then cultured again in medium supplemented with 2 mM TdR for 16 h and switched to TdR-free medium for G1 phase arrest. After being released in fresh medium for 2.5 h, the cells were allowed to progress into the S/G2 phase.

Cell cycle analysis

0.5 × 10^6 cells were collected by trypsinization, washed with cold PBS, and fixed with 70% ice-cold ethanol at 4 °C for at least 12 h. After fixation, cells were washed three times with PBS, and DNA was labeled with propidium iodide (50 μg mL^{-1}) in the presence of RNase A (0.2 mg mL^{-1}, Qiagen #19101) and Triton X-100 (0.01%) for 30 min at RT. Data on DNA content were acquired by BD LSRFortessa™ Cell Analyzer (BD Biosciences) and analyzed using FlowJo v.10 (TreeStar).

DR-GFP and EJ5-GFP reporter assays

To quantify the repair of I-SceI generated DSBs by gene conversion, DR-GFP-/EJ5-GFP-U-2 OS cells were transfected with the indicated siRNAs. After 24 h, cells were transfected with either an empty vector as control or I-SceI expression vector pCBASce, in which RFP was co-expressed. The HR and NHEJ efficiencies were determined by quantifying GFP-positive cells by flow cytometry 48 h post-transfection. MEF cells were transfected with DR-GFP or EJ5-GFP vectors, 24 h later followed by another transfection with RFP co-expressed empty vector or I-SceI vector. Cells were harvested 48 h post transfection and subjected to flow cytometry to examine the GFP signals.

Chromatin IP (ChIP)-qPCR

DR-GFP- and EJ5-GFP-U-2 OS cells were first transfected with the indicated siRNAs, and 24 h later cells were transfected with either an empty vector or I-SceI vector for 48 h. Cells were harvested and fixed with 1% formaldehyde for 10 min at RT. Glycine (125 mM) was added to stop the cross-linking reaction. Chromatin preparation, sonication (shearing chromatin to an average size of ~0.5 kb) and subsequent ChIP were then performed[72]. Briefly, supernatants were incubated with 5 μg corresponding antibodies (Supplementary Table S5) overnight at 4 °C with rocking. Real-time quantitative PCR was performed using a Stratagene M×3005P detection system with SYBR Green incorporated in the primers. Cycling parameters were 95 °C for 5 min, followed by 35 cycles of 95 °C for 30 s, 60 °C for 30 s, and 72 °C for 30 s, and final extension for 7 min at 72 °C. The qPCR primers and antibodies were listed in Supplementary Tables S4 and S5.

Neutral comet assay

The neutral comet assay was performed as previously described[73]. Briefly, single cell suspension was prepared at the concentration of 1 × 10^5 mL^{-1}, then mixed with low-melting agarose (BBI #A600015-0005) at a ratio of 1:7 and spread onto the slides. The gel was allowed to solidify at 4 °C for 10 min. Cells were lysed in lysis buffer (2.5 M NaCl, 100 mM EDTA, 10 mM Tris, 1% N-lauroylsarcosine, and 1% Triton X-100) at RT for 1 h and subjected to DNA unwinding for 20 min. Electrophoresis was performed in electrophoresis buffer (300 mM sodium acetate, 100 mM Tris, pH 8.3) for 30 min at 80 mA. DNA was fixed in 100% ethanol and stained with EB (5 μg mL^{-1}) (Sangon Biotech #A500328-0005). The comet tails were analyzed by Komet 7 comet assay software.

Cell viability measurement

Cell viability assays were conducted as described. 24 h after siRNA knockdown, cells were plated in 96-well plates at densities of 4,000–5,000 cells per well. After another 24 h, cells were treated with varying doses of genotoxic chemicals for 72 h. Following incubation, CellTiter-Glo Reagent

(Promega, USA) was added in a 1:1 ratio to each well and incubated at RT for 10 min. Luminescence was measured using the Tecan Infinite M1000 Pro (Tecan, Männedorf, CHE) and normalized against control cells treated with a vehicle solution.

Cleaved caspase-3 measurement

Cells were harvested and washed with 1 mL of PBS. Fixation was achieved by slowly adding 500 µL of 4% PFA while gently vortexing. After 10 min, cells were washed three times with 1 mL of PBS + 0.3% BSA, and anti-CC3 (Asp175) antibody was applied. Cells were incubated overnight at 4 °C, then washed and incubated in the dark with secondary Alexa Fluor 555 for 1 h, followed by three washes with 1 mL of PBS + 0.3% BSA. Sorting was performed on a BD LSRFortessa™ Cell Analyzer (BD Biosciences) and analyzed using FlowJo v.10 (TreeStar).

Glycerol gradient ultracentrifugation

HsSAGE1 was cloned into a modified pcDNA3.4 vector with 3× Flag tag at the N terminus and transfected into expi293F cells using polyethylenimine (PEI) (Polysciences #26292). The cells were collected after 72 h by centrifugation. The pellets were resuspended in lysis buffer (50 mM HEPES-NaOH, pH 8.0, 150 mM NaCl, 10% glycerol, 1 mM PMSF, 5 mM benzamidine, 2 µg mL^{-1} leupeptin, and 2 µg mL^{-1} pepstatin). The cell suspension was dropped into liquid nitrogen to form cell beads with a diameter of ~10 mm and pulverized to powder by SPEX 6875D Freezer Mill. After the frozen powder thoroughly thawed, the whole cell extract was clarified by centrifugation at 18,000 rpm for 50 min and the supernatant was incubated with anti-DYKDDDDK G1 affinity resin and rocked for 4 h at 4 °C. The proteins were eluted with 0.2 mg mL^{-1} Flag peptides and concentrated for density gradient sedimentation. The concentrated proteins were layered on top of a 12 mL 10–40% (v/v) glycerol gradient in buffer containing 50 mM HEPES-NaOH, pH 8.0, 150 mM NaCl, and centrifuged at 37,000 rpm (SW41 Ti rotor) for 16 h at 4 °C. The fractions, 500 µL each, were collected manually from the top of the gradient and analyzed by SDS-PAGE gel followed by Western blotting with indicated antibodies (Supplementary Table S5).

Expression and purification of human $SAGE1_{SER11-14}$–NuA4 complex

For expression of the NuA4 subcomplex, human EP400 (residues 1,085–2,046, excluding 1,451–1,737) was cloned into a pMal plasmid with an N-terminal MBP tag. Full-length RUVBL1 and RUVBL2 were cloned into a modified petDuet plasmid without any tag. These plasmids were co-expressed in *E. coli* BL21 (DE3). The expression was induced with 0.1 mM IPTG at 18 °C for 18 h, followed by cell harvesting via centrifugation. For *Hs*$SAGE1_{SER11-14}$ (residues 525–716), the corresponding cDNA fragment was cloned into a modified pET28a vector with an N-terminal 6× His-SUMO tag, and transfected into *E. coli* BL21 (DE3). Expression induction and cell harvesting were similar to those described above. Cell pellets were resuspended in a lysis buffer (50 mM HEPES-NaOH, pH 8.0, 150 mM NaCl, 10% glycerol, 1 mM PMSF, 5 mM benzamidine, 1 µg mL^{-1} leupeptin, and 1 µg mL^{-1} pepstatin), mixed, and lysed by sonication. Cellular debris was separated by ultracentrifugation at 40,000× *g* for 40 min. The supernatant was incubated with Amylose Resin (NEB) and rocked at 4 °C for 3 h, followed by elution using 20 mM D-maltose. The eluate was subsequently incubated with Ni-NTA agarose beads (Qiagen) and rocked for 1.5 h at 4 °C followed by elution with 350 mM imidazole. Further purification of the proteins was achieved through gel-filtration chromatography in a buffer of 25 mM HEPES-NaOH, pH 8.0 and 150 mM NaCl. The peak fractions containing the $SAGE1_{SER11-14}$–NuA4 subcomplex were concentrated. Purified sample containing only the NuA4 subcomplex was also obtained following similar procedure.

Expression and purification of human $SAGE1_{IBM}$–SOSS complex

For the expression of the SOSS complex, human INTS3, NABP2 and INIP were cloned into Bac-to-Bac vectors, with an N-terminal glutathione S-transferase (GST) tag for INTS3 and a 6× His-tag for NABP2 and INIP, respectively. Recombinant baculovirus with these constructs was produced in Sf-9 insect cells, and was used to infect High-Five insect cells at a concentration of 2.5×10^6 mL^{-1} with 10 PFU/mL virus. After 72 h the cells were harvested by centrifugation. Lysis and ultracentrifugation steps were identical to those described above, using the same lysis buffer. The supernatant was mixed with glutathione Sepharose-4B beads and rocked for 2 h at 4 °C followed by elution by 25 mM reduced glutathione. Subsequently, the proteins were incubated with Ni-NTA agarose beads and rocked for 1.5 h at 4 °C, and then eluted with 350 mM imidazole. PreScission protease was added to remove the N-terminal 6× His and GST tags. The proteins were further purified by Mono-Q and gel-filtration chromatography steps equilibrated with 50 mM HEPES-NaOH, pH 8.0, and 150 mM NaCl. The purified proteins were concentrated to 10 mg mL^{-1} and stored at −80 °C. For *Hs*$SAGE1_{IBM}$ (residues 818–904), cDNA fragment was cloned into a modified pGEX6p-1 vector with an N-terminal GST tag, and expressed in *E. coli* BL21 (DE3). Expression induction, cell harvesting, lysis and ultracentrifugation steps were similar to those described above, using the same lysis buffer. The supernatant was incubated with glutathione Sepharose-4B beads and rocked for 2 h at 4 °C before eluted using 25 mM reduced glutathione. The protein was further purified by Mono-S and by gel-filtration chromatography steps equilibrated with 25 mM HEPES-NaOH, pH 8.0, and 150 mM NaCl. The purified protein was concentrated to 25 mg mL^{-1} and stored at −80 °C. Purified SOSS complex and GST-$SAGE1_{IBM}$ were mixed at a 1:3 molar ratio and incubated for 30 min on ice. The $SAGE1_{IBM}$–SOSS complex was purified using size-exclusion chromatography on a Superdex 200 column.

Expression and purification of human $SAGE1_{SER11-14}$–CtIP complex

Human CtIP and $SAGE1_{SER11-14}$ were co-expressed in *E. coli* BL21 (DE3) with N-terminal GST and 6× His-SUMO tags, respectively. Expression induction, cell harvesting, lysis and ultracentrifugation steps were similar to those described above, using the same lysis buffer. The supernatant was incubated with Ni-NTA agarose beads for 1.5 h at 4 °C, eluted with 350 mM imidazole, and then mixed with glutathione Sepharose-4B beads for 2 h at 4 °C before elution using 25 mM reduced glutathione. The purified proteins were concentrated and stored at −80 °C.

Evolutionary analysis of DSB repair-related proteins

Proteins related to the DSB repair pathway were manually selected based on our study and previously published papers[11,12]. To estimate the evolutionary patterns of these proteins, we first applied the InParanoiDB (/inparanoidb.sbc.su.se/) database to identify the presence or absence of homologs among 79 species from prokaryotes to primates. For proteins with ambiguous results, we obtained their amino acid/nucleotide sequences from the NCBI database (ncbi.nlm.nih.gov), then conducted BLASTP/BLASTN analyses to determine if there is a homology in a certain species.

Statistical analyses

The statistical details and methods are indicated in the figure legends. Statistical analyses were performed using GraphPad Prism (v9.5.0) or R (v4.2.3) software. Student's *t*-test (parametric) and Wilcoxon rank-sum test (non-parametric) were used to evaluate the statistical significance between two groups. $P < 0.05$ was considered statistically significant. Experiments shown are representative of at least three replicates.

DATA AVAILABILITY

All data are available in the main text, supplementary material, or online storage. Single-cell RNA-seq data reported in this paper have been deposited in the Genome Sequence Archive (Genomics, Proteomics & Bioinformatics 2021) in National Genomics Data Center (Nucleic Acids Res 2022), China National Center for Bioinformation / Beijing Institute of Genomics, Chinese Academy of Sciences (GSA-Human: HRA006321 and CRA014103) and are publicly available as of the date of publication. This paper does not report original code. Any additional information required to reanalyze the data reported in this paper is available upon request.

ACKNOWLEDGMENTS

We thank Hong Lu, Shufang He, Jie Huang, Ying Cui, Rijing Liao, and Yan Cai from Shanghai Jiao Tong University School of Medicine (SHSMU) for help with confocal microscopy and mass spectrometry analyses. We thank Jeremy Stark for reagent assistance. This research was supported by grants from the National Natural Science Foundation of China (31930063 and 32430033 to M.L., 82102765 to J.L., 82072638 to Y.Z., 31971137 to C.H., 32400499 to X.W., 32300609 to T.W.), the Innovative Research Team of High-level Local University in Shanghai (SHSMU-ZLCX20211700 to M.L.), and the National Research Center for Translational Medicine at Shanghai, Ruijin Hospital, Shanghai Jiao Tong University School of Medicine, Shanghai, China (NRCTM(SH)-2021-01 to M.L.). Ming Lei is a SANS Exploration Scholar.

AUTHOR CONTRIBUTIONS

M.L. and J.L. designed the study. M.L., Y.Z. and C.H. supervised the overall research. J.L., X.W., F.W., F.H, and H.L. performed all experiments. H.C., Q.R., X.G., and B.X. collected the tissue samples. X.M., J.C., J.G., L.Z., Y.H., T.W., B.C., Z.B., H.Z., Q.B. and J.W. assisted with experiments. J.L., X.W., C.H. and Y.Z. prepared the data visualizations. M.L., Y.Z., C.H., J.L. and X.W. wrote the manuscript, with input from all authors. All authors edited and approved the final manuscript.

COMPETING INTERESTS

The authors declare no competing interests.

REFERENCES

1. Jackson, S.P. & Bartek, J. The DNA-damage response in human biology and disease. *Nature* **461**, 1071–1078 (2009).
2. Ciccia, A. & Elledge, S.J. The DNA damage response: making it safe to play with knives. *Mol. Cell* **40**, 179–204 (2010).
3. van Gent, D.C., Hoeijmakers, J.H.J. & Kanaar, R. Chromosomal stability and the DNA double-stranded break connection. *Nat. Rev. Genet.* **2**, 196–206 (2001).
4. Mehta, A. & Haber, J.E. Sources of DNA double-strand breaks and models of recombinational DNA repair. *Cold Spring Harb. Perspect. Biol.* **6**, a016428 (2014).
5. Symington, L.S. & Gautier, J. Double-strand break end resection and repair pathway choice. *Annu. Rev. Genet.* **45**, 247–271 (2011).
6. Wright, W.D., Shah, S.S. & Heyer, W.D. Homologous recombination and the repair of DNA double-strand breaks. *J. Biol. Chem.* **293**, 10524–10535 (2018).
7. Thompson, L.H. & Schild, D. Homologous recombinational repair of DNA ensures mammalian chromosome stability. *Mutat. Res.* **477**, 131–153 (2001).
8. Chang, H.H.Y., Pannunzio, N.R., Adachi, N. & Lieber, M.R. Non-homologous DNA end joining and alternative pathways to double-strand break repair. *Nat. Rev. Mol. Cell Biol.* **18**, 495–506 (2017).
9. Ceccaldi, R., Rondinelli, B. & D'Andrea, A.D. Repair pathway choices and consequences at the double-strand break. *Trends Cell Biol.* **26**, 52–64 (2016).
10. Cromie, G.A., Connelly, J.C. & Leach, D.R.F. Recombination at double-strand breaks and DNA ends: conserved mechanisms from phage to humans. *Mol. Cell* **8**, 1163–1174 (2001).
11. Taylor, E.M. & Lehmann, A.R. Conservation of eukaryotic DNA repair mechanisms. *Int. J. Radiat. Biol.* **74**, 277–286 (1998).
12. Arcas, A., Fernández-Capetillo, O., Cases, I. & Rojas, A.M. Emergence and evolutionary analysis of the human DDR network: implications in comparative genomics and downstream analyses. *Mol. Biol. Evol.* **31**, 940–961 (2014).
13. Falck, J., Coates, J. & Jackson, S.P. Conserved modes of recruitment of ATM, ATR and DNA-PKcs to sites of DNA damage. *Nature* **434**, 605–611 (2005).
14. Gupta, R. et al. DNA repair network analysis reveals shieldin as a key regulator of NHEJ and PARP inhibitor sensitivity. *Cell* **173**, 972–988.e23 (2018).
15. Ghezraoui, H. et al. 53BP1 cooperation with the REV7-shieldin complex underpins DNA structure-specific NHEJ. *Nature* **560**, 122–127 (2018).
16. Mirman, Z. et al. 53BP1-RIF1-shieldin counteracts DSB resection through CST- and Polα-dependent fill-in. *Nature* **560**, 112–116 (2018).
17. Noordermeer, S.M. et al. The shieldin complex mediates 53BP1-dependent DNA repair. *Nature* **560**, 117–121 (2018).
18. Dev, H. et al. Shieldin complex promotes DNA end-joining and counters homologous recombination in BRCA1-null cells. *Nat. Cell Biol.* **20**, 954–965 (2018).
19. Barroca, V. & Fouchet, P. Germline stem cells: the first guards of heredity. *Cell Stem Cell* **2**, 108–110 (2008).
20. Talibova, G., Bilmez, Y. & Ozturk, S. DNA double-strand break repair in male germ cells during spermatogenesis and its association with male infertility development. *DNA Repair (Amst)* **118**, 103386 (2022).
21. Murphey, P., McLean, D.J., McMahan, C.A., Walter, C.A. & McCarrey, J.R. Enhanced genetic integrity in mouse germ cells. *Biol. Reprod.* **88**, 6 (2013).
22. Barlow, C. et al. Atm deficiency results in severe meiotic disruption as early as leptonema of prophase I. *Development* **125**, 4007–4017 (1998).
23. Che, L.X., Alavattam, K.G., Stambrook, P.J., Namekawa, S.H. & Du, C.Y. BRUCE preserves genomic stability in the male germline of mice. *Cell Death Differ.* **27**, 2402–2416 (2020).
24. Abe, H. et al. CHEK1 coordinates DNA damage signaling and meiotic progression in the male germline of mice. *Hum. Mol. Genet.* **27**, 1136–1149 (2018).
25. Rübe, C.E., Zhang, S., Miebach, N., Fricke, A. & Rübe, C. Protecting the heritable genome: DNA damage response mechanisms in spermatogonial stem cells. *DNA Repair (Amst)* **10**, 159–168 (2011).
26. Qin, J.C. et al. RAD51 is essential for spermatogenesis and male fertility in mice. *Cell Death Discov.* **8**, 118 (2022).
27. Takubo, K. et al. Stem cell defects in ATM-deficient undifferentiated spermatogonia through DNA damage-induced cell-cycle arrest. *Cell Stem Cell* **2**, 170–182 (2008).
28. Milholland, B. et al. Differences between germline and somatic mutation rates in humans and mice. *Nat. Commun.* **8**, 15183 (2017).
29. Xavier, M.J., Mitchell, L.A., McEwan, K.E., Scott, R.J. & Aitken, R.J. Genomic integrity in the male germ line: evidence in support of the disposable soma

hypothesis. *Reproduction* **156**, 269–282 (2018).

30. Moore, L. et al. The mutational landscape of human somatic and germline cells. *Nature* **597**, 381–386 (2021).
31. Lindsay, S.J., Rahbari, R., Kaplanis, J., Keane, T. & Hurles, M.E. Similarities and differences in patterns of germline mutation between mice and humans. *Nat. Commun.* **10**, 4053 (2019).
32. Shao, Y. et al. GenTree, an integrated resource for analyzing the evolution and function of primate-specific coding genes. *Genome Res.* **29**, 682–696 (2019).
33. Shami, A.N. et al. Single-cell RNA sequencing of human, macaque, and mouse testes uncovers conserved and divergent features of mammalian spermatogenesis. *Dev. Cell* **54**, 529–547.e12 (2020).
34. Lau, X., Munusamy, P., Ng, M.J. & Sangrithi, M. Single-cell RNA sequencing of the *Cynomolgus* macaque testis reveals conserved transcriptional profiles during mammalian spermatogenesis. *Dev. Cell* **54**, 548–566.e7 (2020).
35. Bellutti, L. et al. Genome-wide transcriptional silencing and mRNA stabilization allow the coordinated expression of the meiotic program in mice. *Nucleic Acids Res.* **53**, gkaf146 (2025).
36. Wang, H.L., Peng, Z., Li, Y.Q., Lai, J.Y. & Wang, L. *Rosa26* locus is inactive in spermatogenesis of C57BL/6 mice. *Integr. Med. Nephrol. Androl.* **10**, e00015 (2023).
37. Feng, L.J., Shi, Z., Xie, J., Ma, B.B. & Chen, X. Enhancer of polycomb maintains germline activity and genome integrity in *Drosophila* testis. *Cell Death Differ.* **25**, 1486–1502 (2018).
38. Lang, F.C. et al. CTCF prevents genomic instability by promoting homologous recombination-directed DNA double-strand break repair. *Proc. Natl. Acad. Sci. USA* **114**, 10912–10917 (2017).
39. D'Amours, D. & Jackson, S.P. The MRE11 complex: at the crossroads of DNA repair and checkpoint signalling. *Nat. Rev. Mol. Cell Biol.* **3**, 317–327 (2002).
40. Deshpande, R.A. et al. DNA-dependent protein kinase promotes DNA end processing by MRN and CtIP. *Sci. Adv.* **6**, eaay0922 (2020).
41. Reginato, G. & Cejka, P. The MRE11 complex: a versatile toolkit for the repair of broken DNA. *DNA Repair (Amst)* **91–92**, 102869 (2020).
42. You, Z.S. et al. CtIP links DNA double-strand break sensing to resection. *Mol. Cell* **36**, 954–969 (2009).
43. Zdravković, A. et al. A conserved Ctp1/CtIP C-terminal peptide stimulates Mre11 endonuclease activity. *Proc. Natl. Acad. Sci. USA* **118**, e2016287118 (2021).
44. Sartori, A.A. et al. Human CtIP promotes DNA end resection. *Nature* **450**, 509–514 (2007).
45. Zou, L.E. & Elledge, S.J. Sensing DNA damage through ATRIP recognition of RPA-ssDNA complexes. *Science* **300**, 1542–1548 (2003).
46. Huang, J., Gong, Z.H., Ghosal, G. & Chen, J.J. SOSS complexes participate in the maintenance of genomic stability. *Mol. Cell* **35**, 384–393 (2009).
47. Skaar, J.R. et al. INTS3 controls the hSSB1-mediated DNA damage response. *J. Cell Biol.* **187**, 25–32 (2009).
48. Vidhyasagar, V. et al. Biochemical characterization of INTS3 and C9ORF80, two subunits of hNABP1/2 heterotrimeric complex in nucleic acid binding. *Biochem. J.* **475**, 45–60 (2018).
49. El-Kamand, S. et al. The molecular details of a novel phosphorylation-dependent interaction between MRN and the SOSS complex. *Protein Sci.* **32**, e4782 (2023).
50. Long, Q.L. et al. The phosphorylated trimeric SOSS1 complex and RNA polymerase II trigger liquid-liquid phase separation at double-strand breaks. *Cell Rep.* **42**, 113489 (2023).
51. Doyon, Y. & Côté, J. The highly conserved and multifunctional NuA4 HAT complex. *Curr. Opin. Genet. Dev.* **14**, 147–154 (2004).
52. Qu, K.K., Chen, K.J., Wang, H., Li, X.M. & Chen, Z.C. Structure of the NuA4 acetyltransferase complex bound to the nucleosome. *Nature* **610**, 569–574 (2022).
53. Zhang, F., Ma, T. & Yu, X.C. A core hSSB1-INTS complex participates in the DNA damage response. *J. Cell Sci.* **126**, 4850–4855 (2013).
54. Richard, D.J. et al. Single-stranded DNA-binding protein hSSB1 is critical for genomic stability. *Nature* **453**, 677–681 (2008).
55. Yang, S.H. et al. The SOSS1 single-stranded DNA binding complex promotes DNA end resection in concert with Exo1. *EMBO J.* **32**, 126–139 (2013).
56. Murr, R. et al. Histone acetylation by Trrap-Tip60 modulates loading of repair proteins and repair of DNA double-strand breaks. *Nat. Cell Biol.* **8**, 91–99 (2006).
57. Ikura, T. et al. Involvement of the TIP60 histone acetylase complex in DNA repair and apoptosis. *Cell* **102**, 463–473 (2000).
58. Dhar, S., Gursoy-Yuzugullu, O., Parasuram, R. & Price, B.D. The tale of a tail: histone H4 acetylation and the repair of DNA breaks. *Philos. Trans. R. Soc. Lond. B Biol. Sci.* **372**, 20160284 (2017).
59. Jacquet, K. et al. The TIP60 complex regulates bivalent chromatin recognition by 53BP1 through direct H4K20me binding and H2AK15 acetylation. *Mol. Cell* **62**, 409–421 (2016).
60. Clarke, T.L. et al. PRMT5-dependent methylation of the TIP60 coactivator RUVBL1 is a key regulator of homologous recombination. *Mol. Cell* **65**, 900–916.e7 (2017).
61. Tang, J.B. et al. Acetylation limits 53BP1 association with damaged chromatin to promote homologous recombination. *Nat. Struct. Mol. Biol.* **20**, 317–325 (2013).
62. Qiu, L.Y. et al. The HDAC6-RNF168 axis regulates H2A/H2A.X ubiquitination to enable double-strand break repair. *Nucleic Acids Res.* **51**, 9166–9182 (2023).
63. Sun, Y.L., Jiang, X.F., Chen, S.J., Fernandes, N. & Price, B.D. A role for the Tip60 histone acetyltransferase in the acetylation and activation of ATM. *Proc. Natl. Acad. Sci. USA* **102**, 13182–13187 (2005).
64. Ford, E.A., Beckett, E.L., Roman, S.D., McLaughlin, E.A. & Sutherland, J.M. Advances in human primordial follicle activation and premature ovarian insufficiency. *Reproduction* **159**, R15–R29 (2020).
65. Cardoso-Moreira, M. et al. Gene expression across mammalian organ development. *Nature* **571**, 505–509 (2019).
66. Huang, R.X. & Zhou, P.K. DNA damage repair: historical perspectives, mechanistic pathways and clinical translation for targeted cancer therapy. *Signal Transduct. Target. Ther.* **6**, 254 (2021).
67. Stanic, M. & Mekhail, K. Integration of DNA damage responses with dynamic spatial genome organization. *Trends Genet.* **38**, 290–304 (2022).
68. Guo, J.T. et al. Chromatin and single-cell RNA-Seq profiling reveal dynamic signaling and metabolic transitions during human spermatogonial stem cell development. *Cell Stem Cell* **21**, 533–546.e6 (2017).
69. Ibtisham, F. et al. The optimized condition for the isolation and *in vitro* propagation of mouse spermatogonial stem cells. *Biol. Futur.* **70**, 79–87 (2019).
70. Baazm, M. et al. An improved protocol for isolation and culturing of mouse spermatogonial stem cells. *Cell Reprogram.* **15**, 329–336 (2013).
71. Green, C.D. et al. A comprehensive roadmap of murine spermatogenesis defined by single-cell RNA-Seq. *Dev. Cell* **46**, 651–667.e10 (2018).
72. Kim, T.H. & Dekker, J. ChIP-quantitative polymerase chain reaction (ChIP-qPCR). *Cold Spring Harb. Protoc.* **2018**, 354–355 (2018).
73. Li, J.Z. et al. Genome integrity and neurogenesis of postnatal hippocampal neural stem/progenitor cells require a unique regulator Filia. *Sci. Adv.* **6**, eaba0682 (2020).

ADDITIONAL INFORMATION

Supplementary information The online version contains supplementary material available at https://doi.org/10.15302/vita.2026.05.0034.

Correspondence and requests for materials should be addressed to Chenhui Huang, Yanjie Zhang, or Ming Lei.

Reprints and permission information is available at https://www.vita-journal.com/.